Enhanced Energy Storage Performance of Confined Co-Doping Dielectric Films via Nanoparticle Self-Assembly in Ferroelectric Phases

Kun Xing[1,2], Qi-Ze Han[1], Jian-Tao Wang[1], Lei Huang[1], Zhaoyu Ran[1], Li-Juan Yin[1], Shao-Long Zhong[1], Jingtong Lu[2], Baoquan Wan[1], Xin-Jie Wang[1], Limin Guo*[2], Ke Bi*[2], Zhi-Min Dang*[1,3]

[1]State Key Laboratory of Power System Operation and Control, Department of Electrical Engineering, Tsinghua University, Beijing, China.

[2]State Key Laboratory of Information Photonics and Optical Communications, School of Physical Science and Technology, Beijing University of Posts and Telecommunications, Beijing, China.

[3]Zhongyuan Electric Laboratory, Xuchang, Henan, China

*Corresponding author(s). E-mail(s): dangzm@tsinghua.edu.cn; bike@bupt.edu.cn; guolimin@bupt.edu.cn

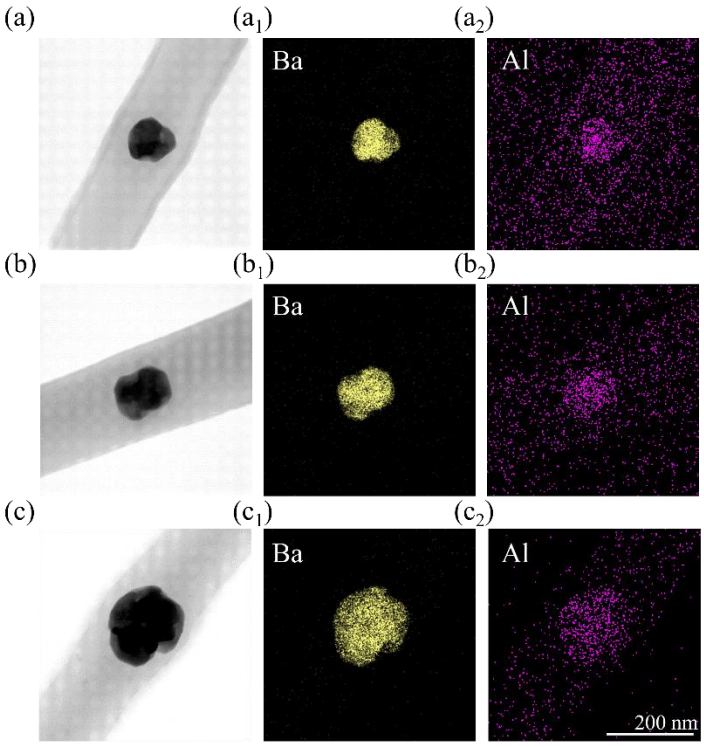

Fig. S1. TEM images of the core co-doped fibers: 1 wt% $BaTiO_3$/1 wt% Al_2O_3 (a-a_2), 1 wt% $BaTiO_3$/2 wt% Al_2O_3 (b-b_2), and 1 wt% $BaTiO_3$/3 wt% Al_2O_3 (c-c_2).

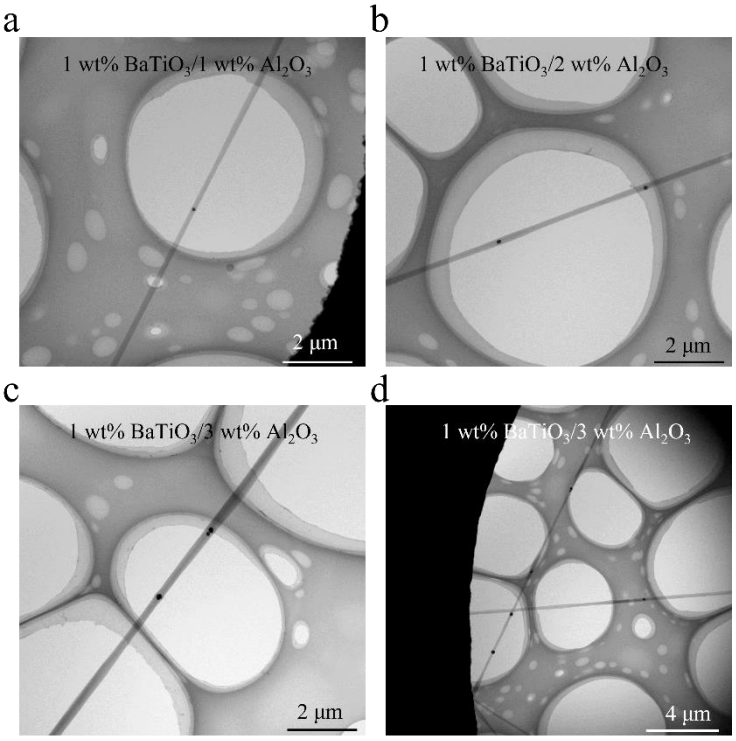

Fig. S2. TEM image of the core co-doped fiber at low magnification.

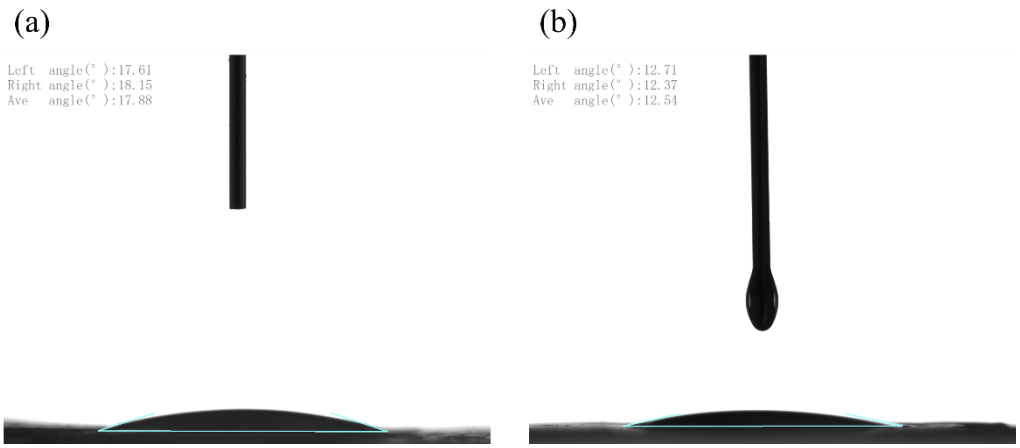

Fig. S3. Contact angle tests of (a) water and (b) n-hexadecane with $BaTiO_3$ surface.

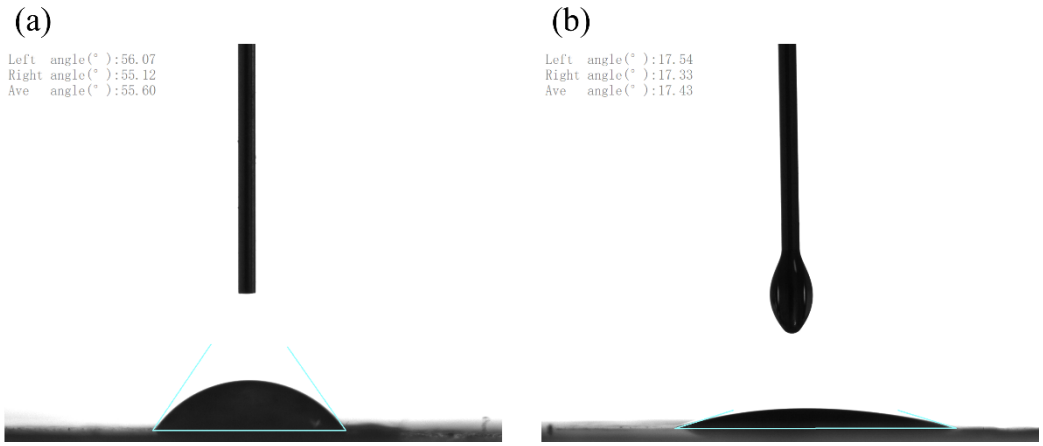

Fig. S4. Contact angle tests of (a) water and (b) n-hexadecane with Al_2O_3 surface.

Fig. S5. Surface tension test of P(VDF-HFP)/DMF solution.

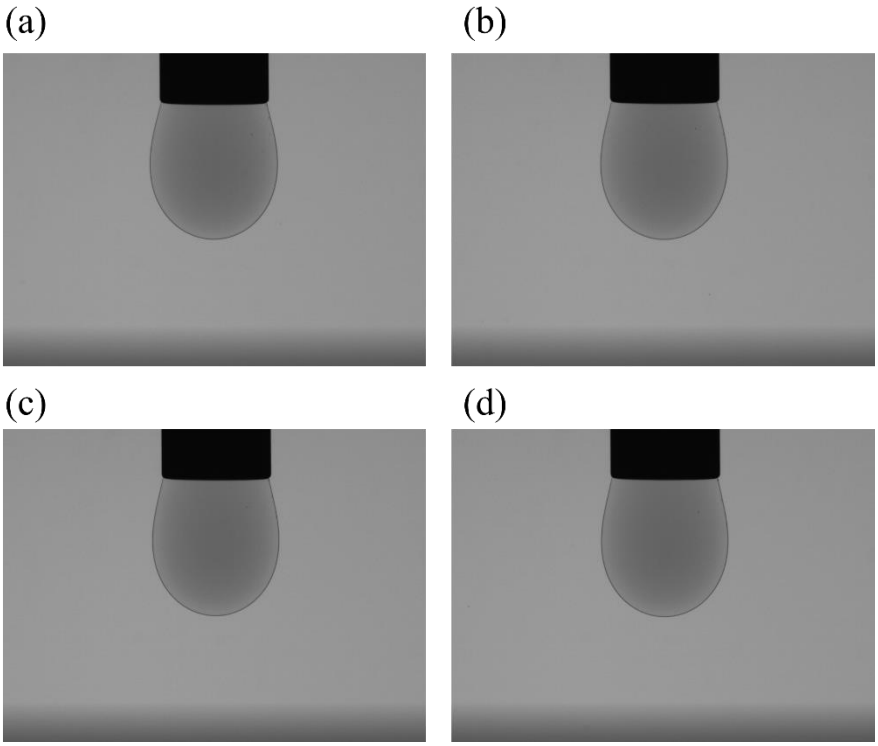

Fig. S6. Interfacial tension tests of P(VDF-HFP)/DMF solutions at (a) 0 s, (b) 60 s, (c) 120 s and (d) 180 s.

Table S1. Surface free energy and corresponding components of $BaTiO_3$ nanoparticles.

$BaTiO_3$	Solid Surface Free Energy	Solid Polar Force	Solid Dispersion Forces
	69.90 mN/m	42.96 mN/m	26.95 mN/m
Polarity Test Liquid	water	Non-polar Test Liquid	n-Hexadecane
Contact Angle of Polarity Test Fluid	17.88°	Contact Angle of Non-polar Test Fluid	12.54°

Table S2. Surface free energy and corresponding components of Al_2O_3 nanoparticles.

Al_2O_3	Solid Surface Free Energy	Solid Polar Force	Solid Dispersion Forces
	47.7 mN/m	21.35 mN/m	26.35 mN/m
Polarity Test Liquid	water	Non-polar Test Liquid	n-Hexadecane
Contact Angle of Polarity Test Fluid	55.6°	Contact Angle of Non-polar Test Fluid	17.43°

Table S3. Surface tension of P(VDF-HFP)/DMF solution.

Run-No.	time (sec)	γ (mN/m)
1	1558.573	30.88
2	1558.573	30.76
3	1641.622	30.88
4	1716.037	30.93
5	1726.69	30.85

Table S4. Interfacial tension between P(VDF-HFP)/DMF solution and n-hexadecane.

Run-No.	time (sec)	γ (mN/m)	Run-No.	time (sec)	γ (mN/m)
72	142	2.87	82	162	2.87
73	144	2.88	83	164	2.87
74	146	2.88	84	166	2.87
75	148	2.88	85	168	2.86
76	150	2.87	86	170	2.86
77	152	2.87	87	172	2.86
78	154	2.87	88	174	2.86
79	156	2.87	89	176	2.86
80	158	2.87	90	178	2.86
81	160	2.87	91	180	2.86

Table S5. Surface tension and corresponding components of n-hexadecane. (Provided by the database of the test system)

Surface tension	Dispersion Component	Polar Component
27.47 mN/m	27.47 mN/m	0

Table S6. Calculated surface tension and corresponding components of P(VDF-HFP)/DMF solution.

Surface tension	Dispersion Component	Polar Component
30.93 mN/m	28.08 mN/m	2.85 mN/m

Table S7. Calculated interfacial free energy between different components.

Interfacial Free Energy of $BaTiO_3$-Al_2O_3	Interfacial Free Energy of $BaTiO_3$-P(VDF-HFP)/DMF Solution	Interfacial Free Energy of the Al_2O_3-P(VDF-HFP)/DMF Solution
3.7	23.7	8.6

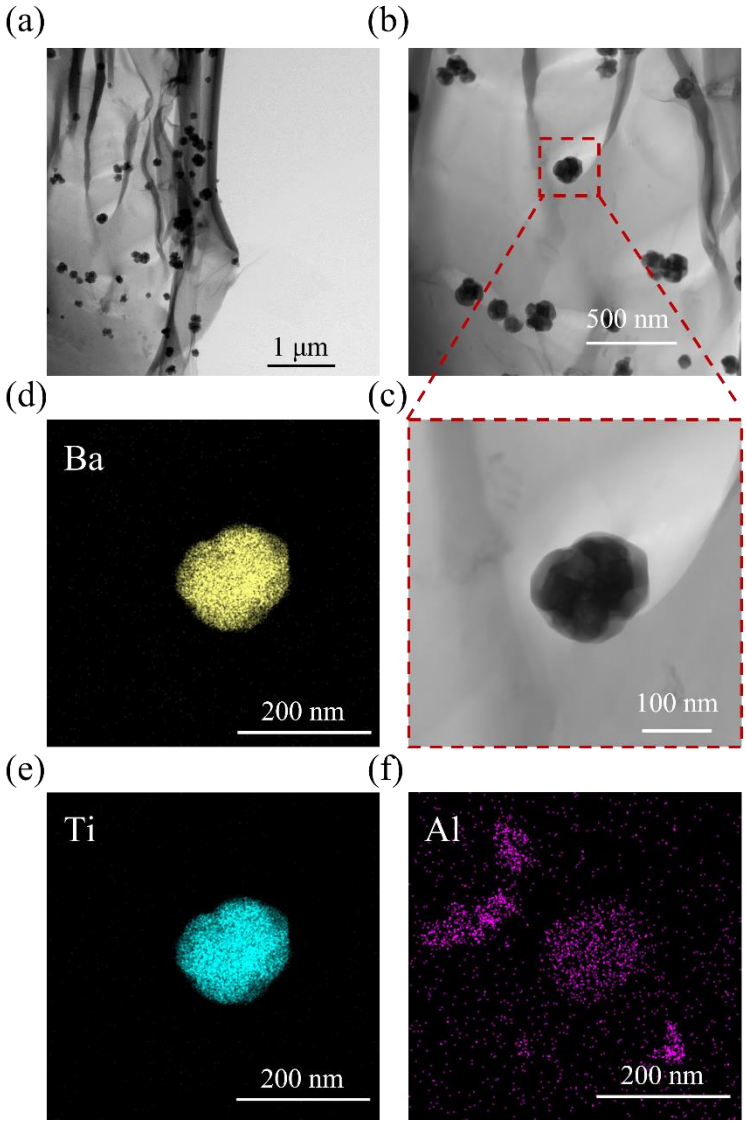

Fig. S7. TEM and EDS images of 1 wt% $BaTiO_3$/1 wt% Al_2O_3-P (VDF-HFP) dielectric prepared by the casting method.

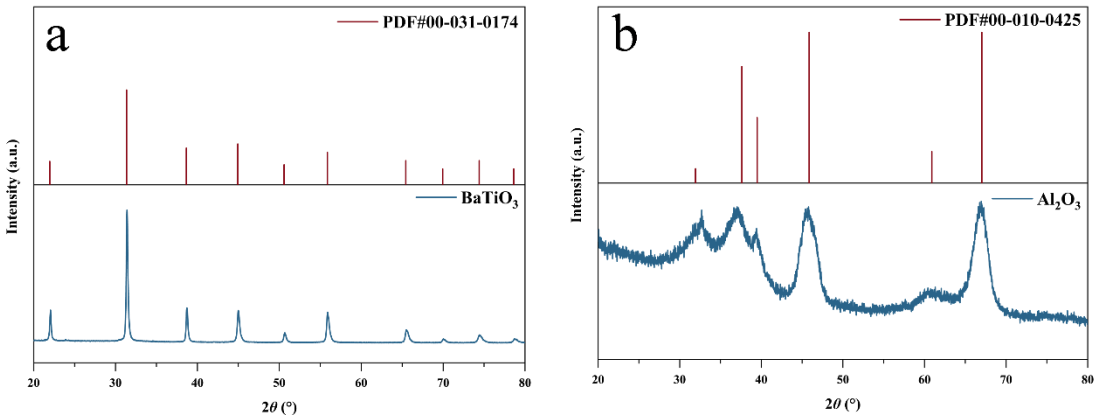

Fig. S8. XRD patterns of (a) $BaTiO_3$ and (b) Al_2O_3 nanoparticles compared with standard reference patterns.

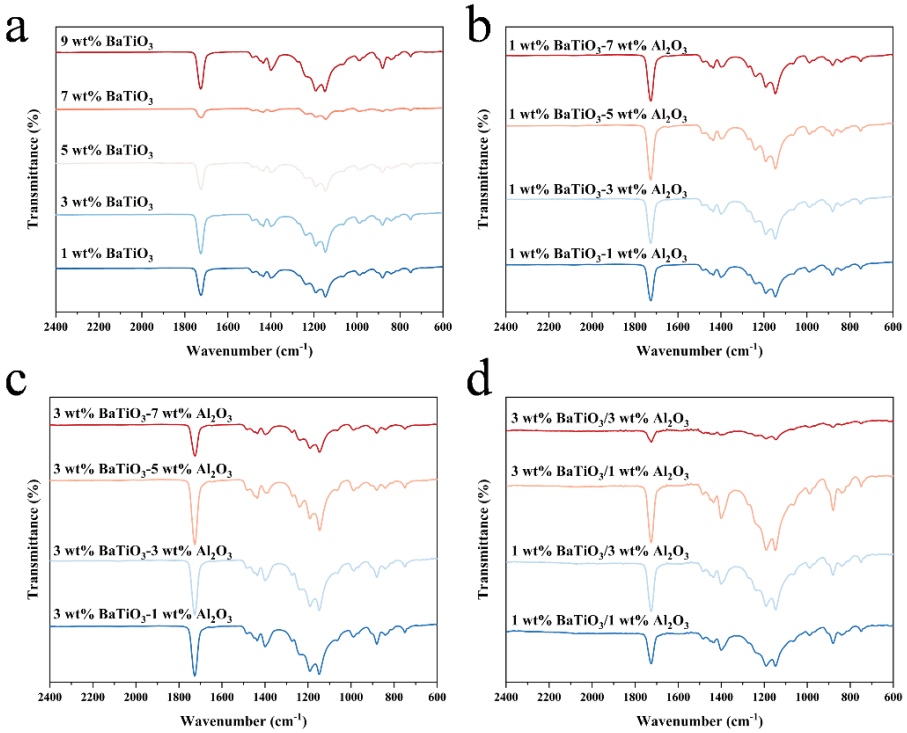

Fig. S9. FTIR spectra of (a) core-doped $BaTiO_3$ dielectric, (b,c) layered-doped dielectrics, and (d) core co-doped dielectric.

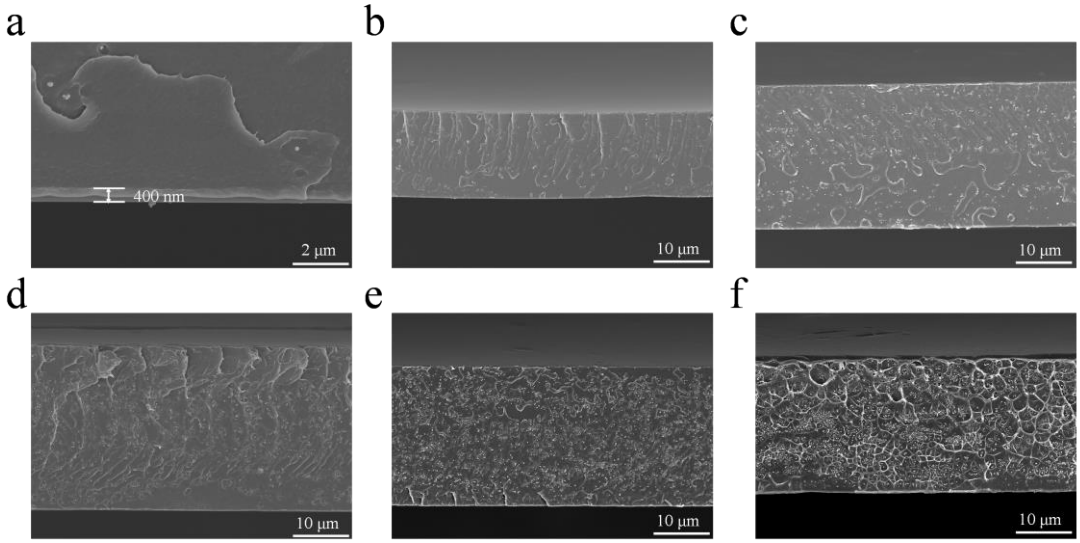

Fig. S10. (a) Thickness of the PMMA surface layer in core-doped $BaTiO_3$ dielectrics. Cross-sectional SEM images of core-doped $BaTiO_3$ dielectrics at doping levels of (b) 1 wt% $BaTiO_3$, (c) 3 wt% $BaTiO_3$, (d) 5 wt% $BaTiO_3$, (e) 7 wt% $BaTiO_3$, and (f) 9 wt% $BaTiO_3$.

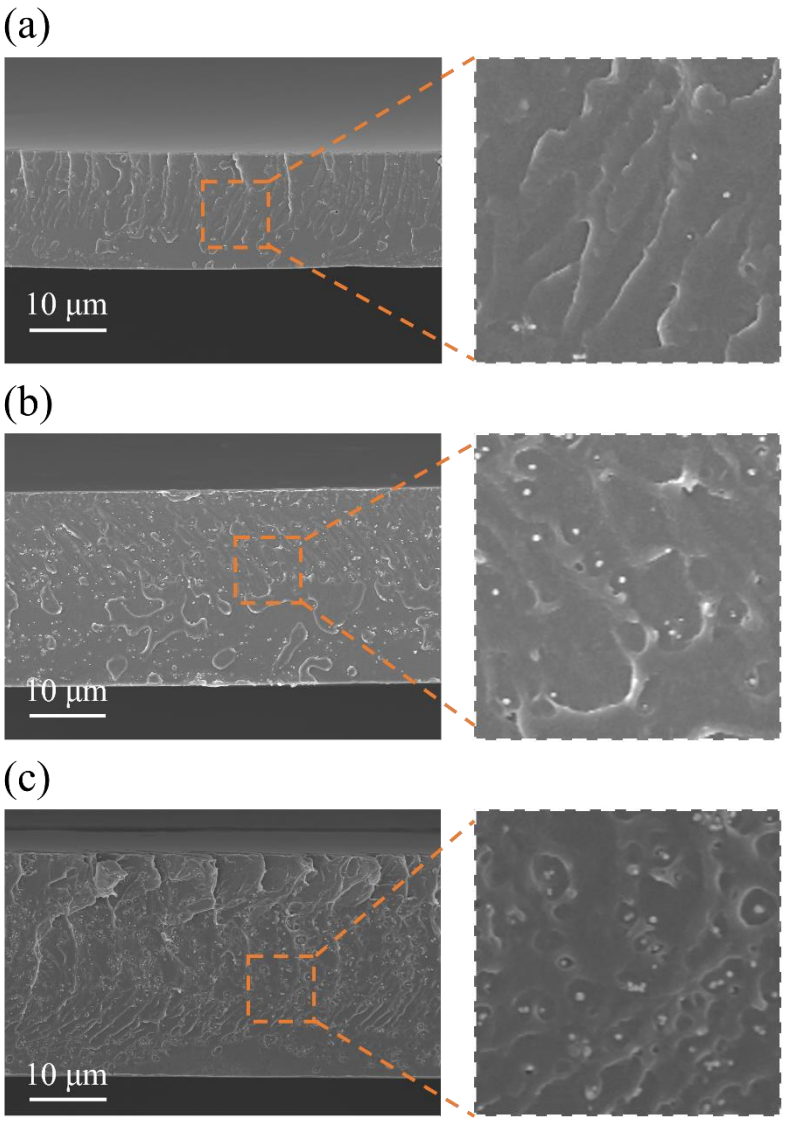

Fig. S11. Inorganic particle density analysis inside (a) 1 wt% $BaTiO_3$ dielectric, (b) 3 wt% $BaTiO_3$ dielectric and (c) 5 wt% $BaTiO_3$ dielectric.

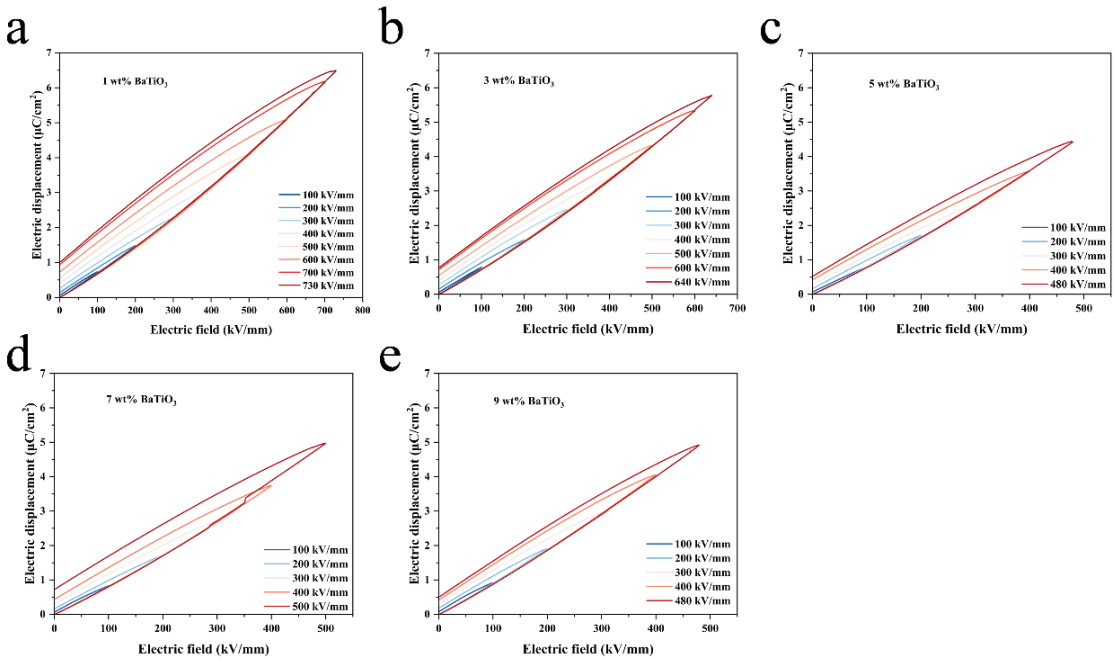

Fig. S12. *D-E* curves of core-doped $BaTiO_3$ dielectrics at doping levels of (a) 1 wt% $BaTiO_3$, (b) 3 wt% $BaTiO_3$, (c) 5 wt% $BaTiO_3$, (d) 7 wt% $BaTiO_3$, and (e) 9 wt% $BaTiO_3$ under different electric fields.

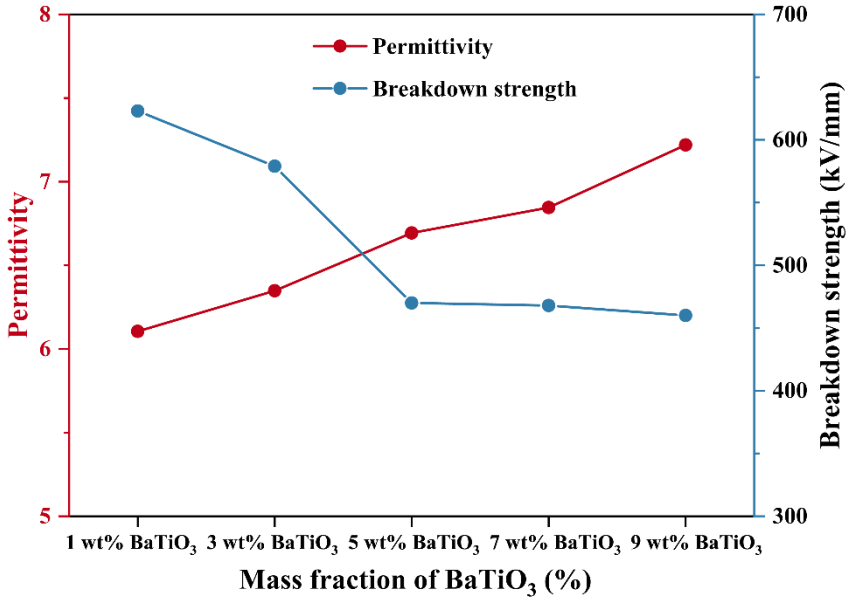

Fig. S13. Trends of the dielectric constant and breakdown strength of core-doped $BaTiO_3$ dielectrics as a function of doping levels.

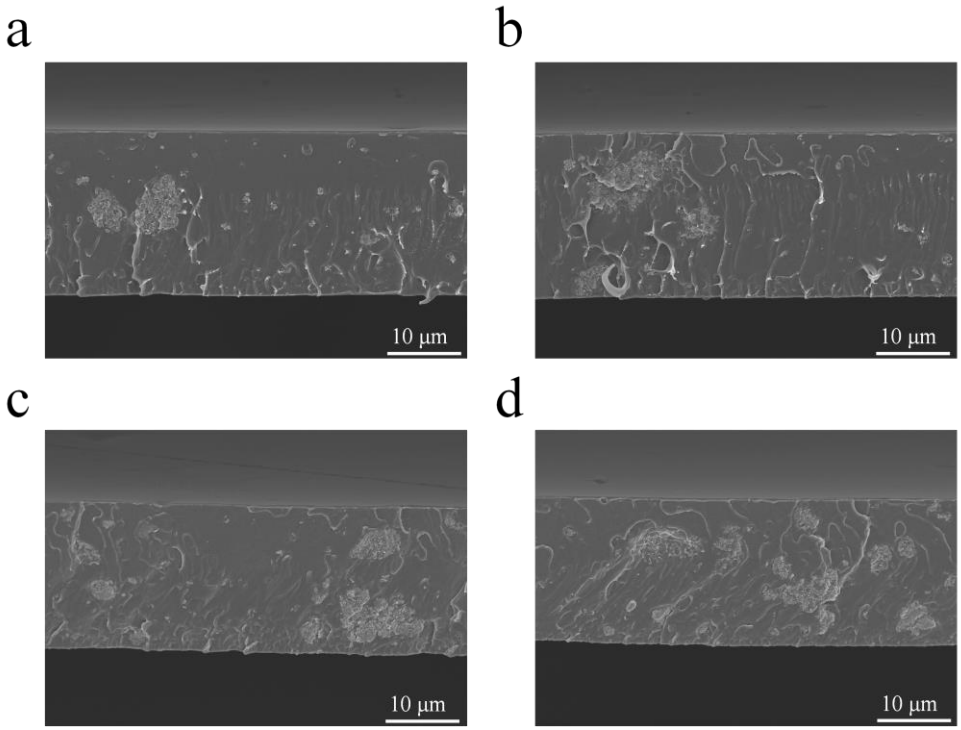

Fig. S14. Cross-sectional SEM images of layered-doped dielectrics: (a) 1 wt% $BaTiO_3$-1 wt% Al_2O_3, (b) 1 wt% $BaTiO_3$-3 wt% Al_2O_3, (c) 1 wt% $BaTiO_3$-5 wt% Al_2O_3, and (d) 1 wt% $BaTiO_3$-7 wt% Al_2O_3.

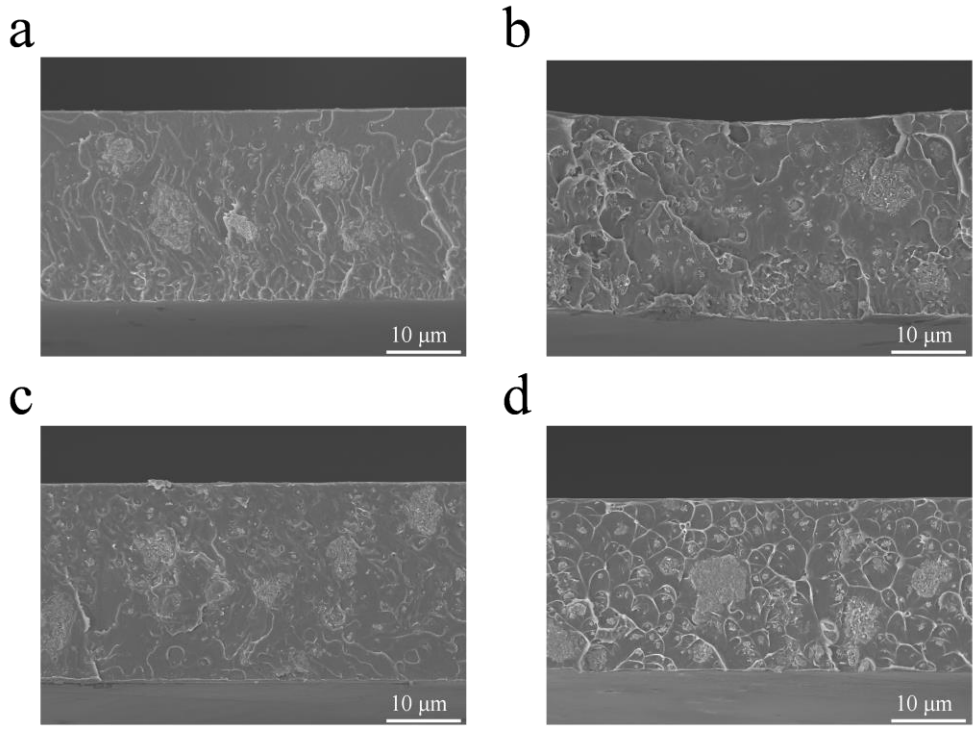

Fig. S15. Cross-sectional SEM images of layered-doped dielectrics: (a) 3 wt% $BaTiO_3$-1 wt% Al_2O_3, (b) 3 wt% $BaTiO_3$-3 wt% Al_2O_3, (c) 3 wt% $BaTiO_3$-5 wt% Al_2O_3, and (d) 3 wt% $BaTiO_3$-7 wt% Al_2O_3.

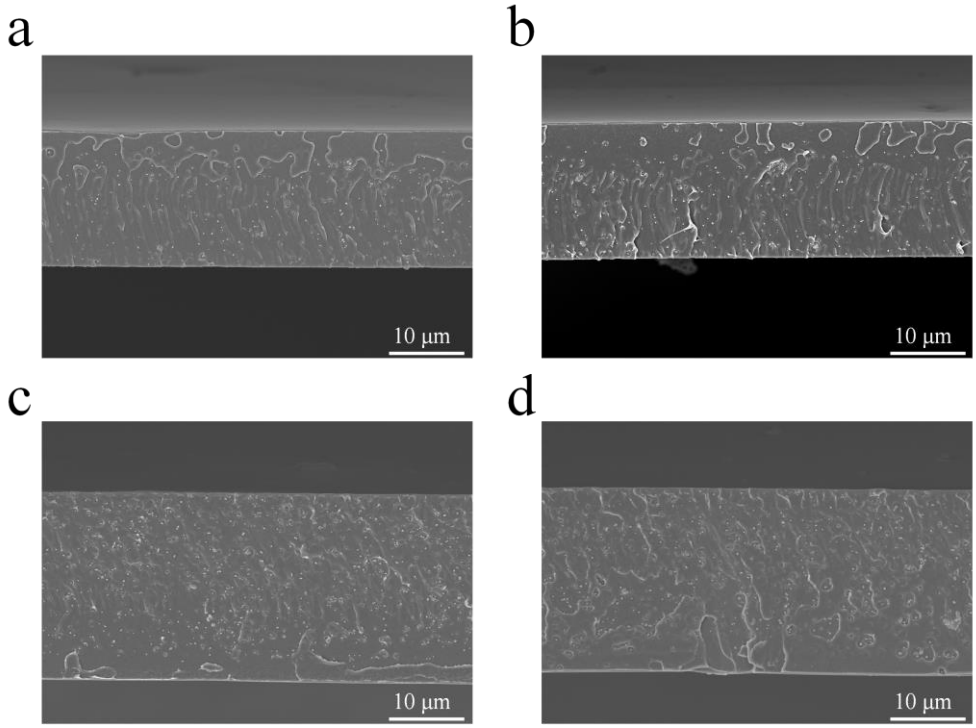

Fig. S16. Cross-sectional SEM images of core co-doped dielectrics: (a) 1 wt% $BaTiO_3$/1 wt% Al_2O_3, (b) 1 wt% $BaTiO_3$/3 wt% Al_2O_3, (c) 3 wt% $BaTiO_3$/1 wt% Al_2O_3, and (d) 3 wt% $BaTiO_3$/3 wt% Al_2O_3.

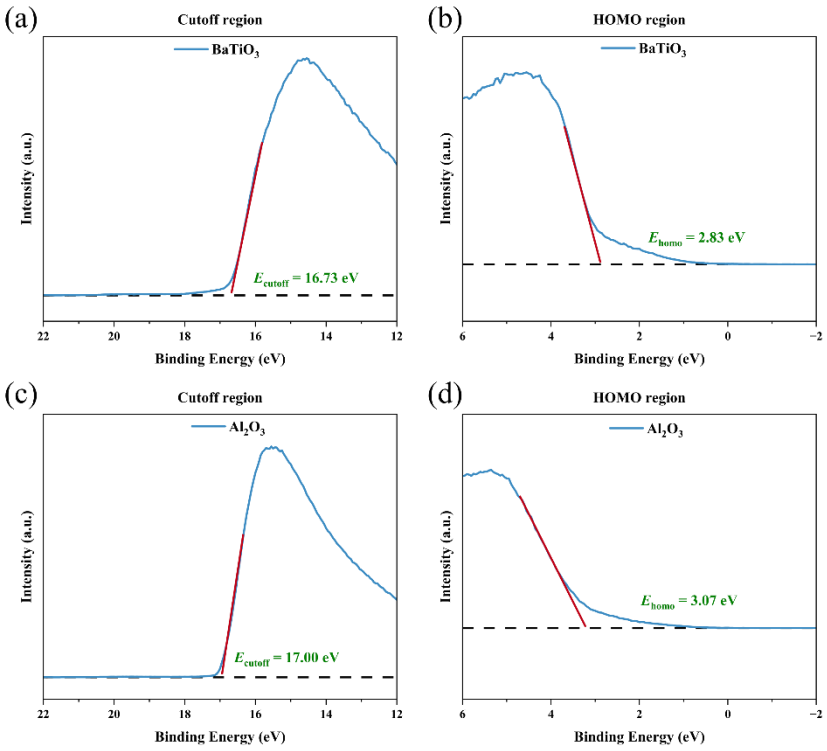

Fig. S17. Ultraviolet photoelectron spectra of $BaTiO_3$ and Al_2O_3. Cutoff region of (a) $BaTiO_3$ and (c) Al_2O_3, HOMO region of (b) $BaTiO_3$ and (d) Al_2O_3. The UPS results show that, under an incident photon energy of $h\nu$ = 21.2 eV, the work functions of $BaTiO_3$ and Al_2O_3 are 4.47 eV and 4.20 eV, respectively, while their highest occupied energy levels (HOMO) are 2.83 eV and 3.07 eV, respectively. Accordingly, the ionization potentials of $BaTiO_3$ and Al_2O_3 were calculated to be 7.30 eV and 7.27 eV.

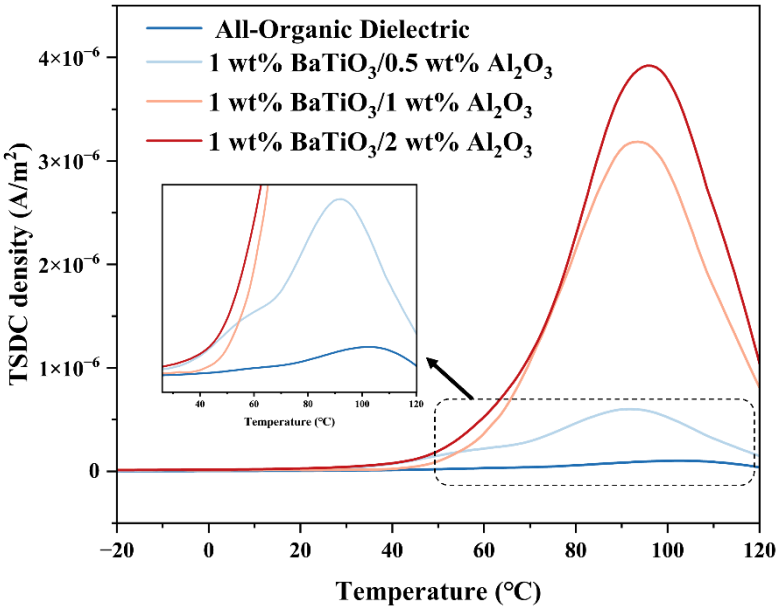

Fig. S18. Thermally Stimulated Depolarization Current of all-organic dielectric and core co-doped dielectric.

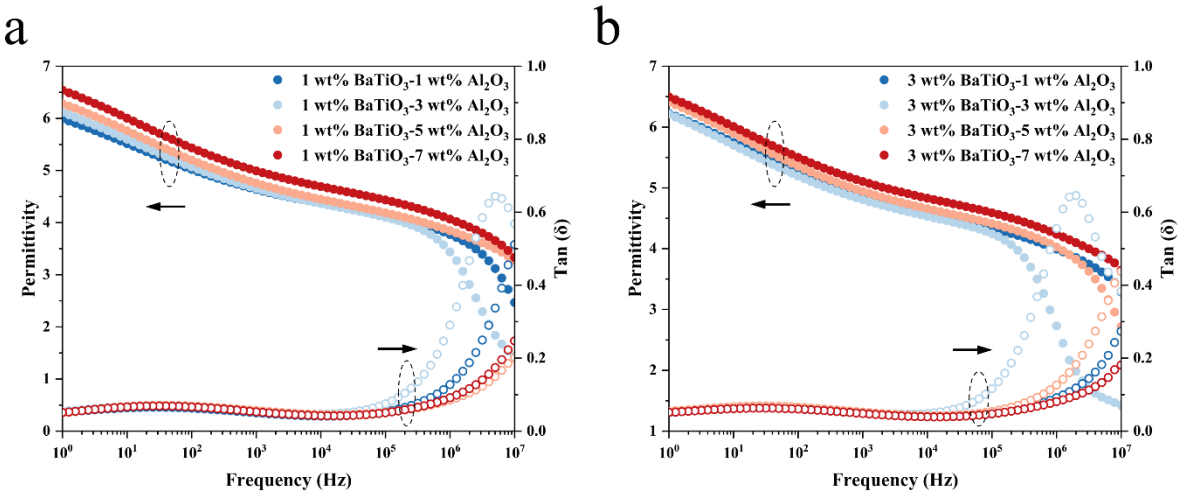

Fig. S19. Frequency-dependent dielectric constant and dielectric loss of layered-doped dielectrics: (a) 1 wt% $BaTiO_3$-*x* wt% Al_2O_3 and (b) 3 wt% $BaTiO_3$-*x* wt% Al_2O_3.

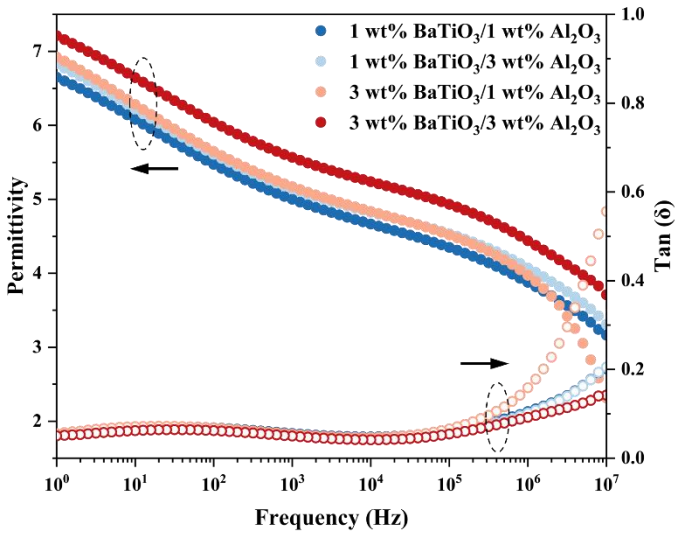

Fig. S20. Frequency-dependent dielectric constant and dielectric loss of core co-doped dielectrics.

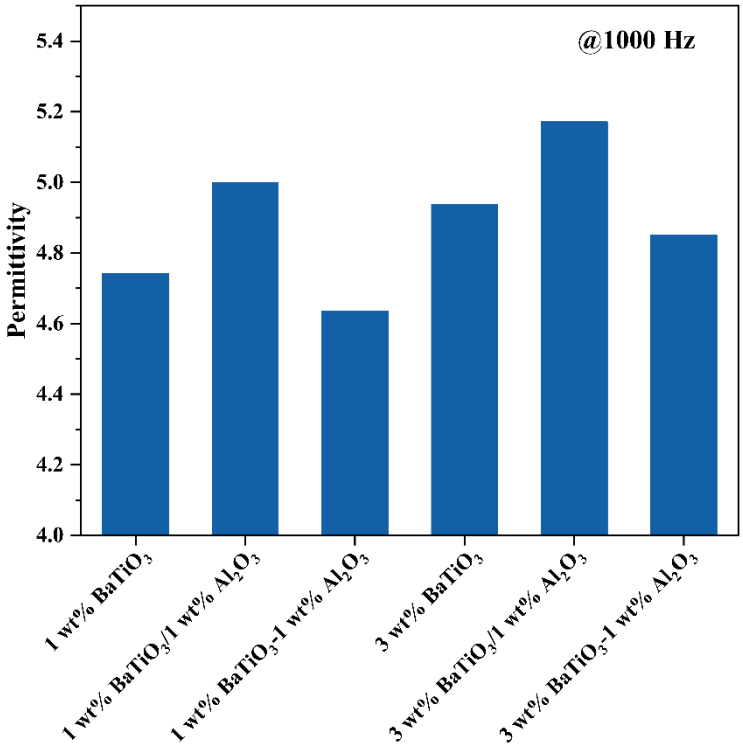

Fig. S21. Dielectric constants of core-doped $BaTiO_3$ dielectric and co-doped dielectric at 1000 Hz

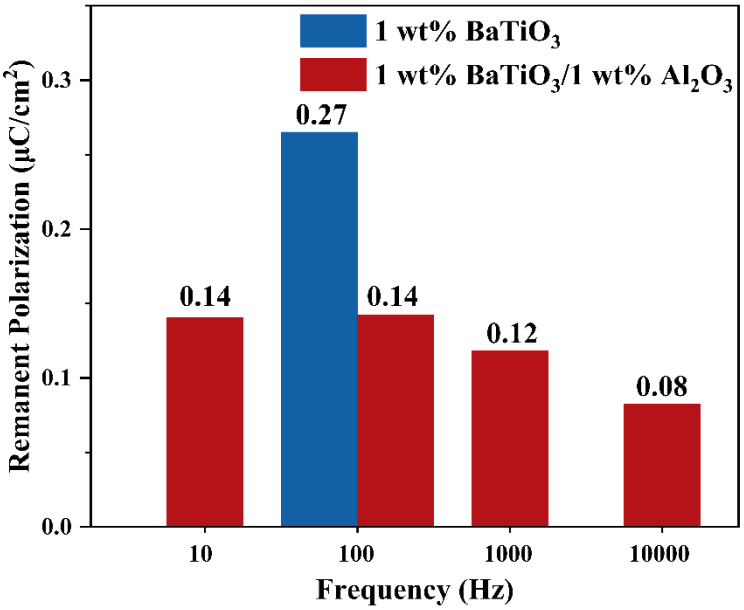

Fig. S22. Remanent polarization intensities of 1 wt% $BaTiO_3$ and 1 wt% $BaTiO_3$/1 wt% Al_2O_3 dielectrics at 10 Hz, 100 Hz, 1000 Hz and 10000 Hz.

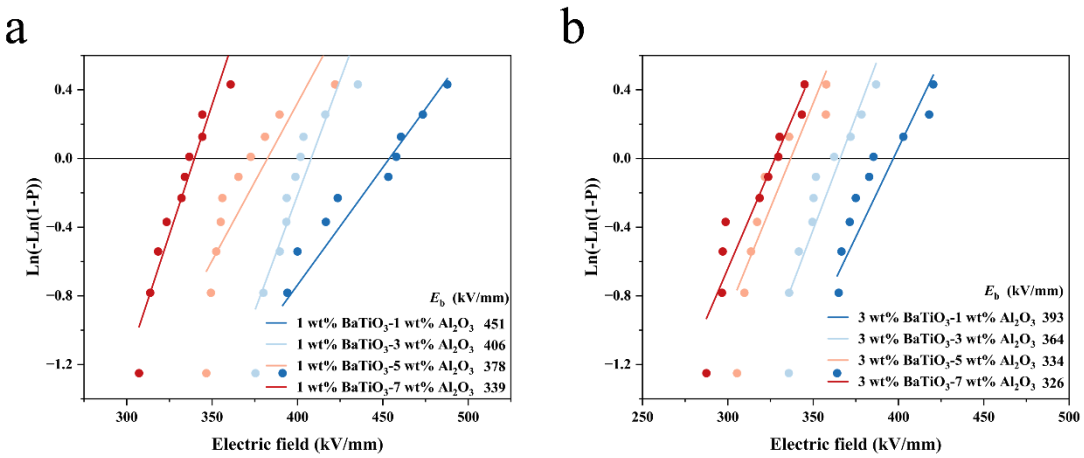

Fig. S23. Breakdown strength of layered-doped dielectrics: (a) 1 wt% $BaTiO_3$-*x* wt% Al_2O_3 and (b) 3 wt% $BaTiO_3$-*x* wt% Al_2O_3.

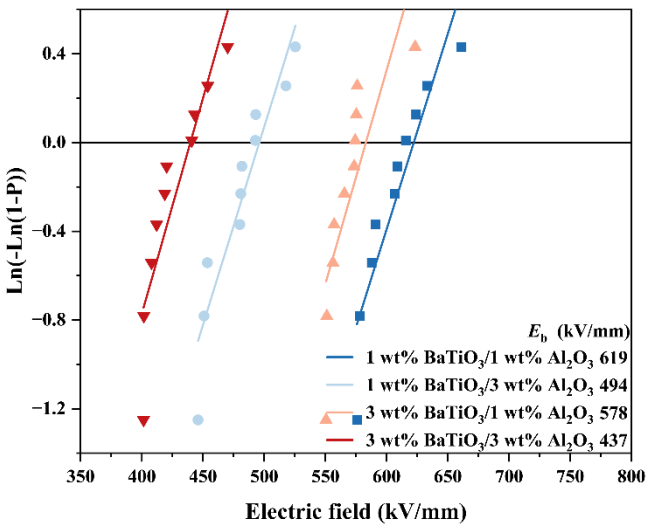

Fig. S24. Breakdown strength of core co-doped dielectrics.

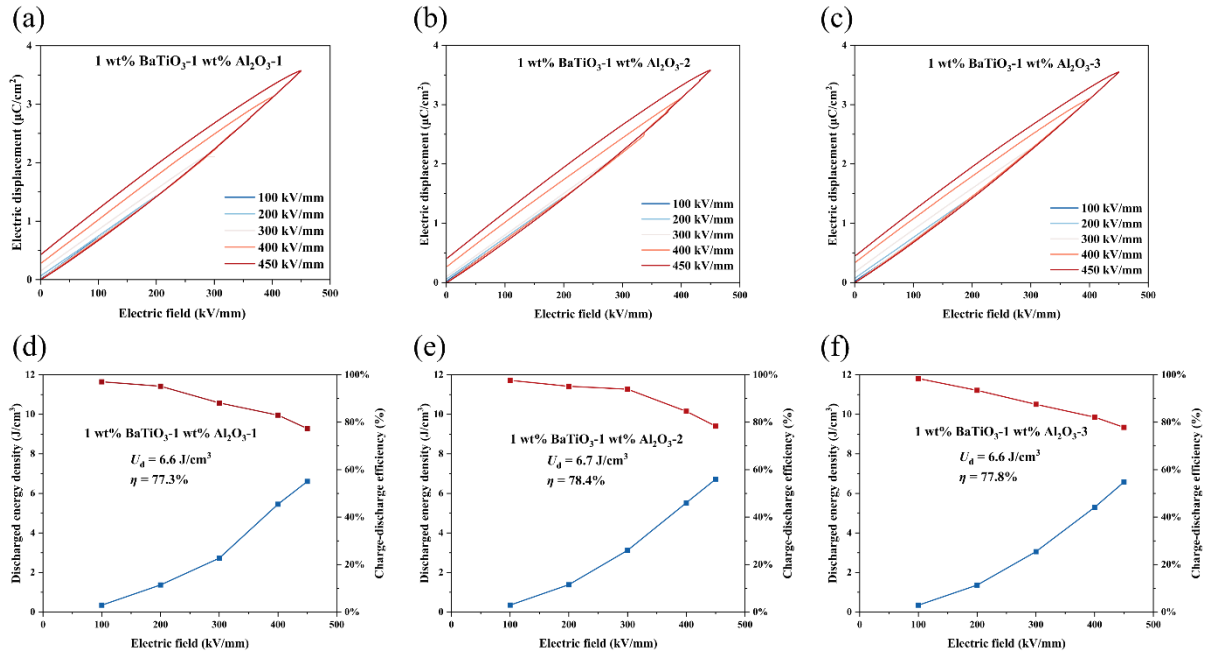

Fig. S25. (a-c) *D-E* curves and (d-f) discharged energy density and charge-discharge efficiency of layered-doped dielectric 1 wt% $BaTiO_3$-1 wt% Al_2O_3.

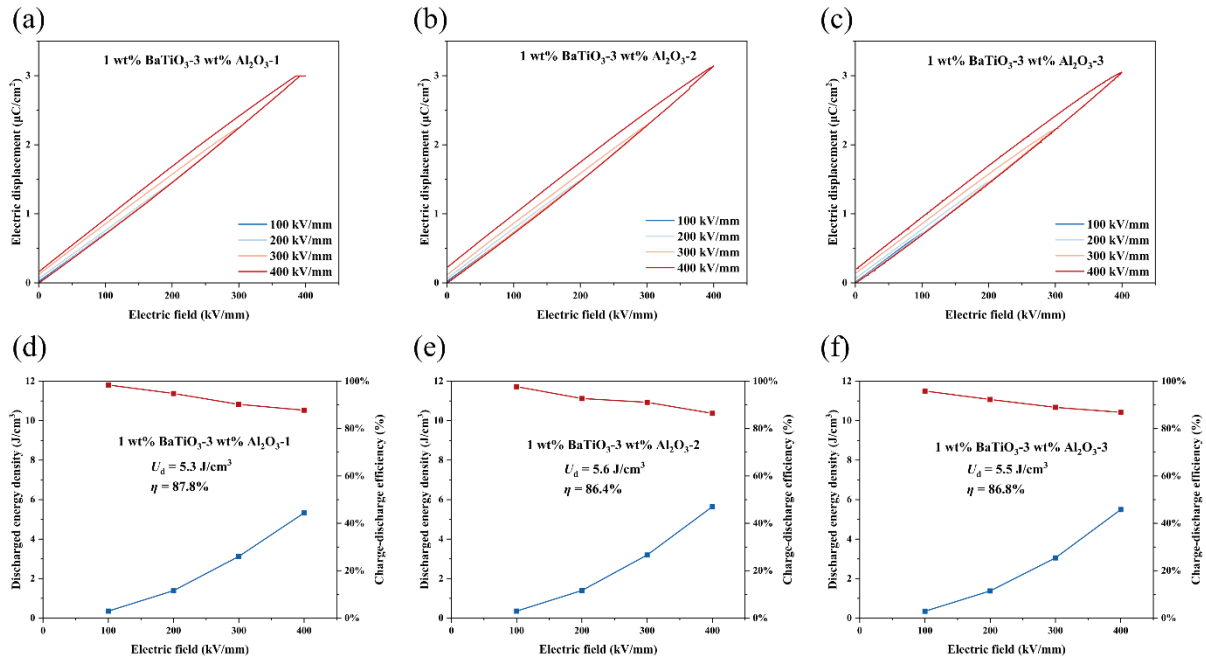

Fig. S26. (a-c) *D-E* curves and (d-f) discharged energy density and charge-discharge efficiency of layered-doped dielectric 1 wt% $BaTiO_3$-3 wt% Al_2O_3.

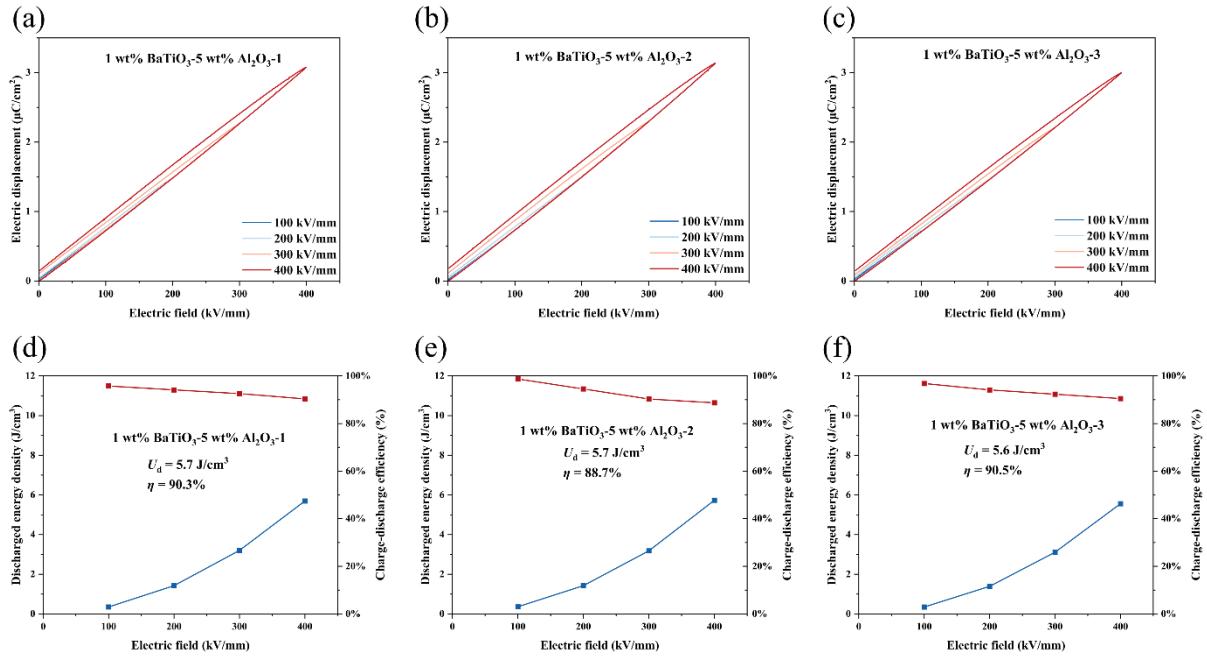

Fig. S27. (a-c) *D-E* curves and (d-f) discharged energy density and charge-discharge efficiency of layered-doped dielectric 1 wt% $BaTiO_3$-5 wt% Al_2O_3.

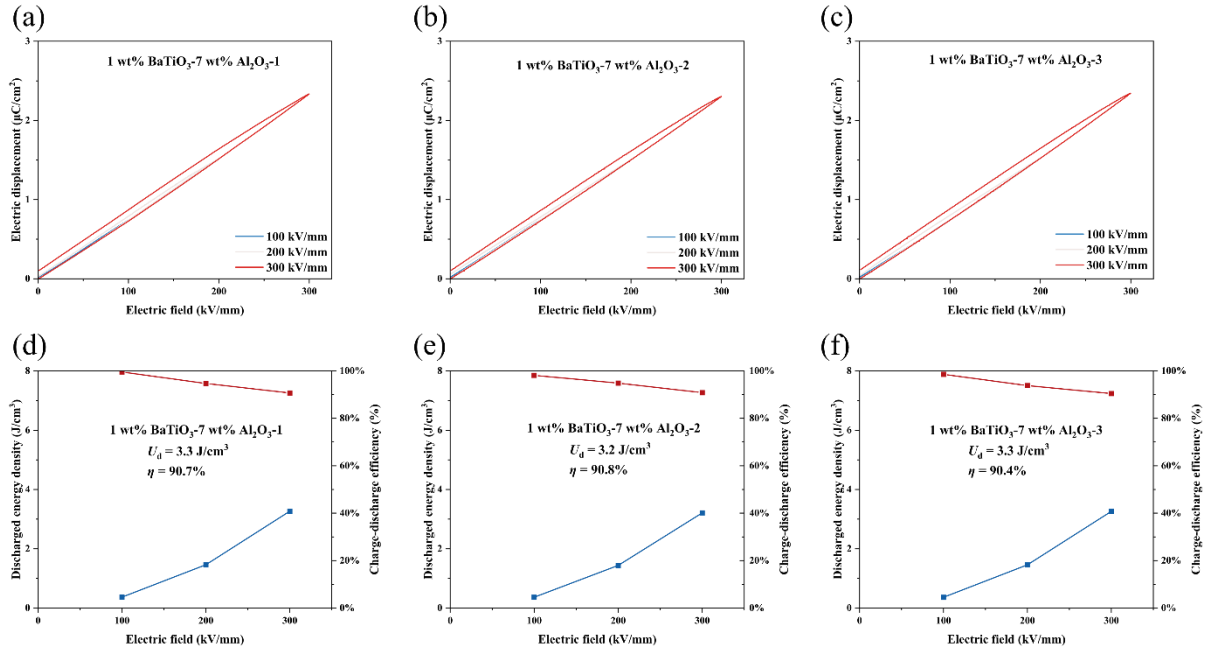

Fig. S28. (a-c) *D-E* curves and (d-f) discharged energy density and charge-discharge efficiency of layered-doped dielectric 1 wt% $BaTiO_3$-7 wt% Al_2O_3.

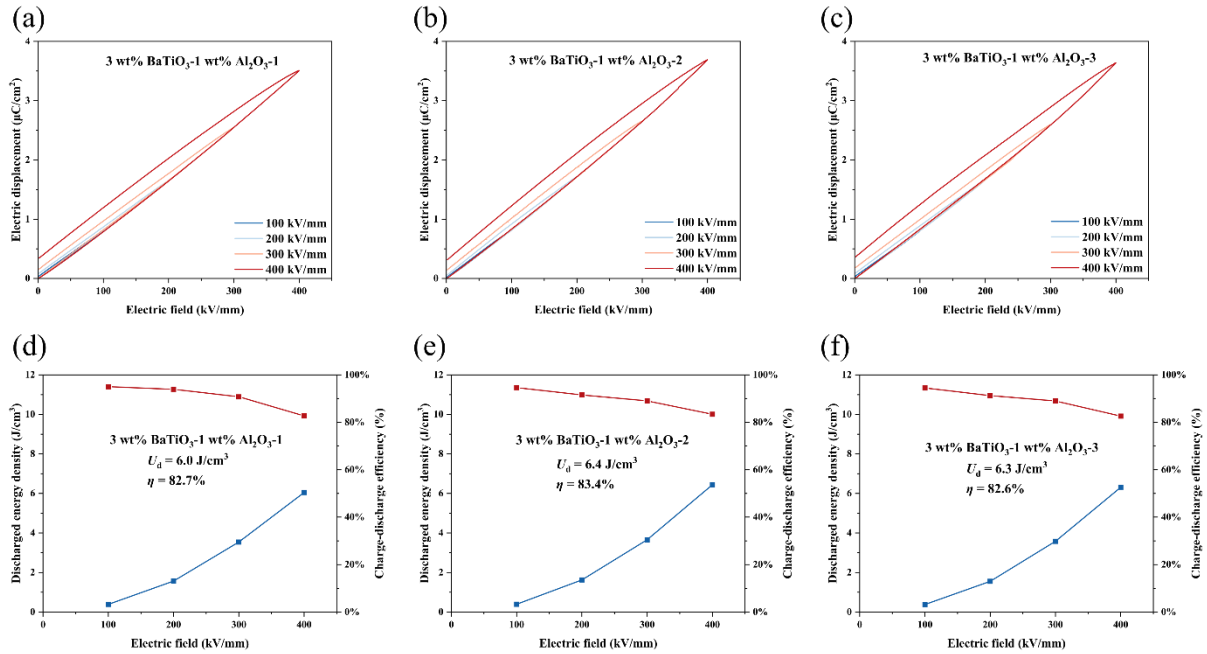

Fig. S29. (a-c) *D-E* curves and (d-f) discharged energy density and charge-discharge efficiency of layered-doped dielectric 3 wt% $BaTiO_3$-1 wt% Al_2O_3.

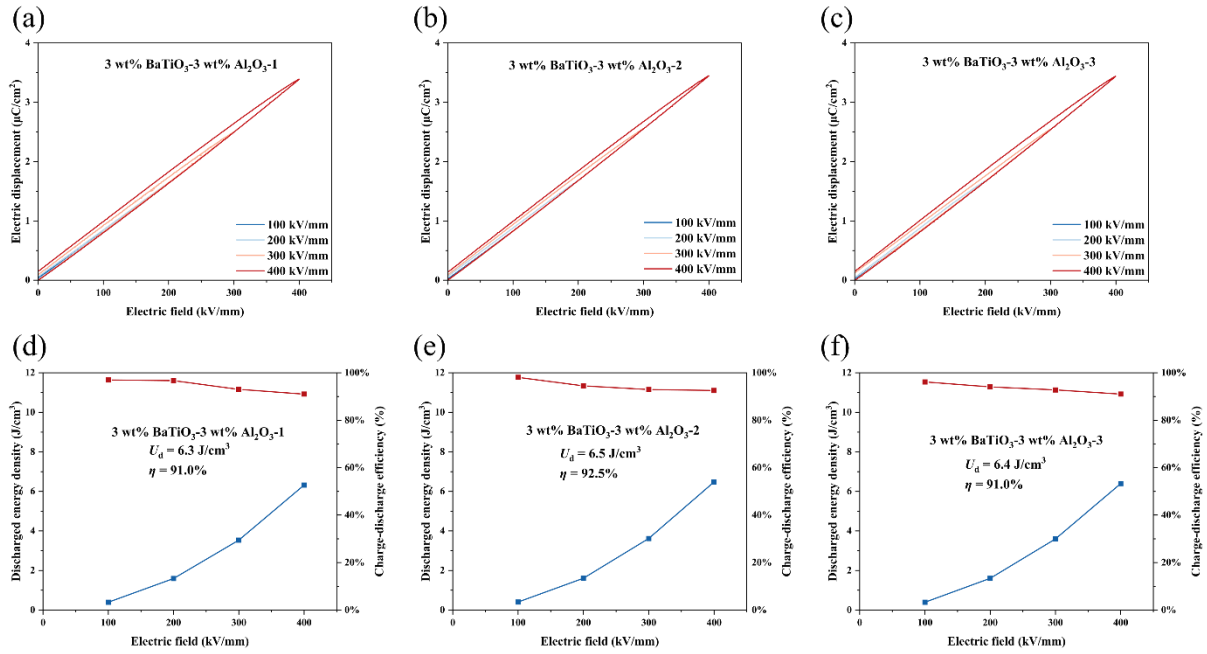

Fig. S30. (a-c) *D-E* curves and (d-f) discharged energy density and charge-discharge efficiency of layered-doped dielectric 3 wt% $BaTiO_3$-3 wt% Al_2O_3.

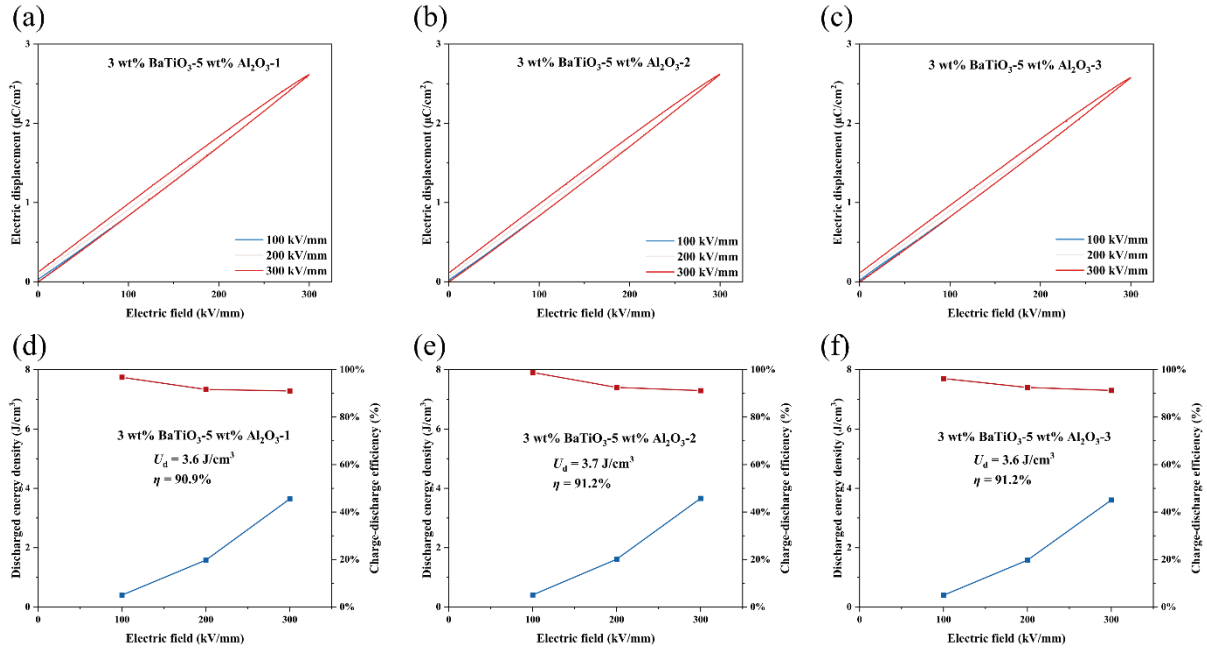

Fig. S31. (a-c) *D-E* curves and (d-f) discharged energy density and charge-discharge efficiency of layered-doped dielectric 3 wt% $BaTiO_3$-5 wt% Al_2O_3.

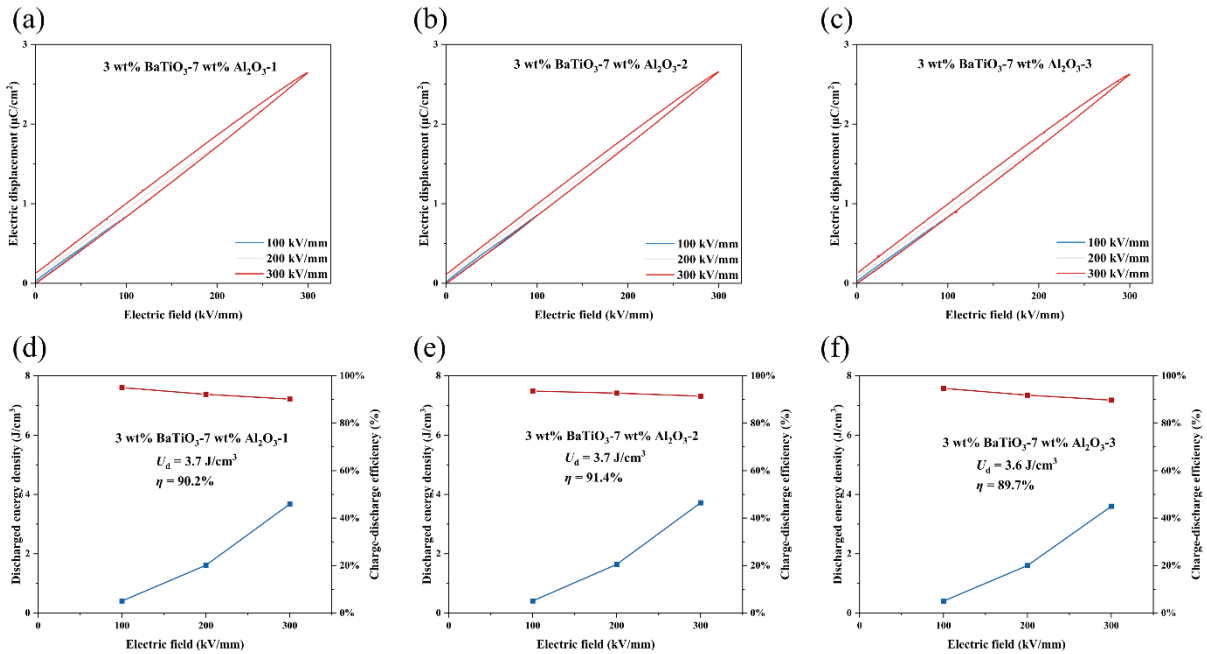

Fig. S32. (a-c) *D-E* curves and (d-f) discharged energy density and charge-discharge efficiency of layered-doped dielectric 3 wt% $BaTiO_3$-7 wt% Al_2O_3.

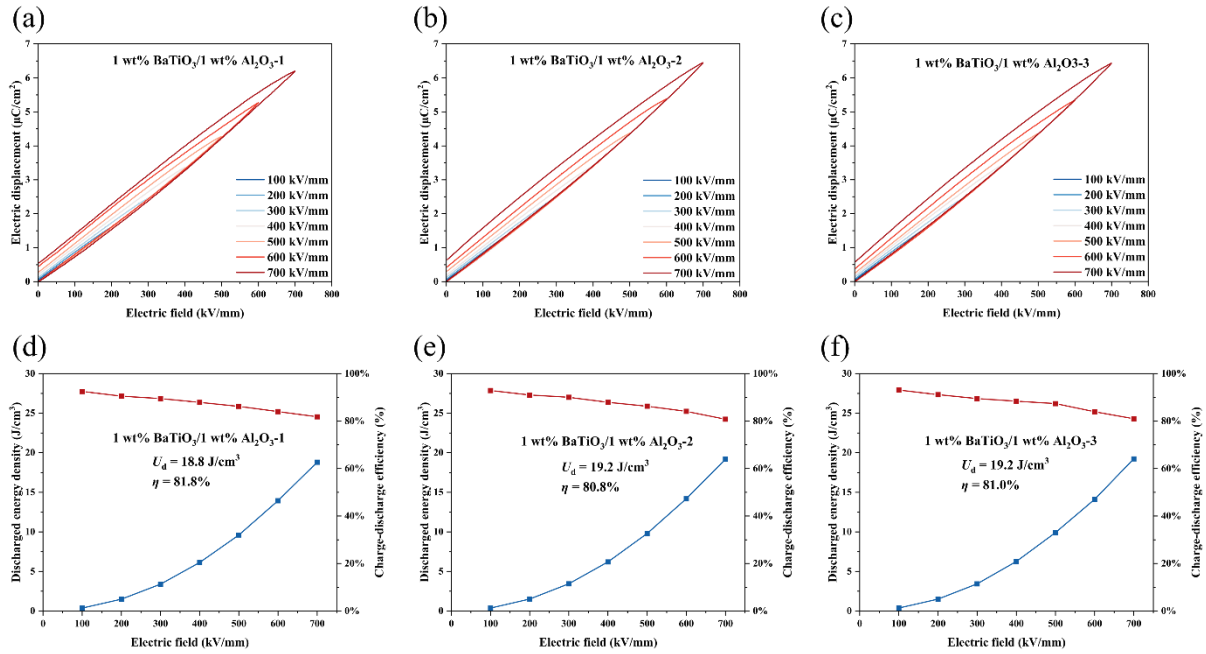

Fig. S33. (a-c) *D-E* curves and (d-f) discharged energy density and charge-discharge efficiency of the core co-doped dielectric 1 wt% $BaTiO_3$/1 wt% Al_2O_3.

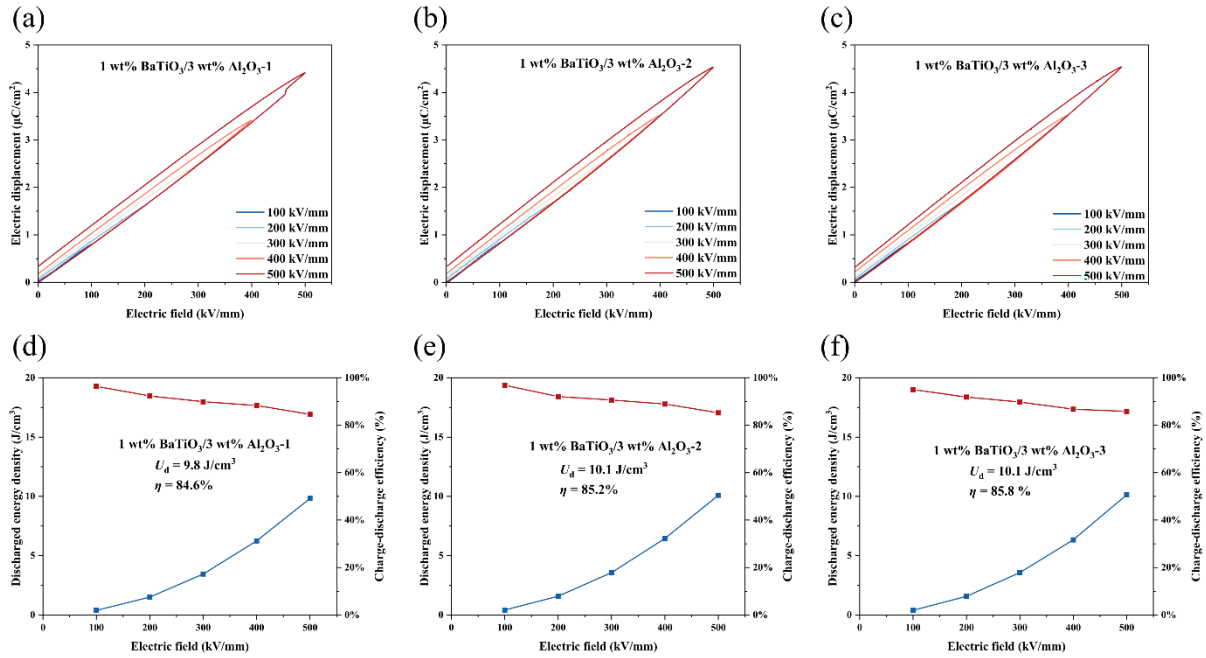

Fig. S34. (a-c) *D-E* curves and (d-f) discharged energy density and charge-discharge efficiency of the core co-doped dielectric 1 wt% $BaTiO_3$/3 wt% Al_2O_3.

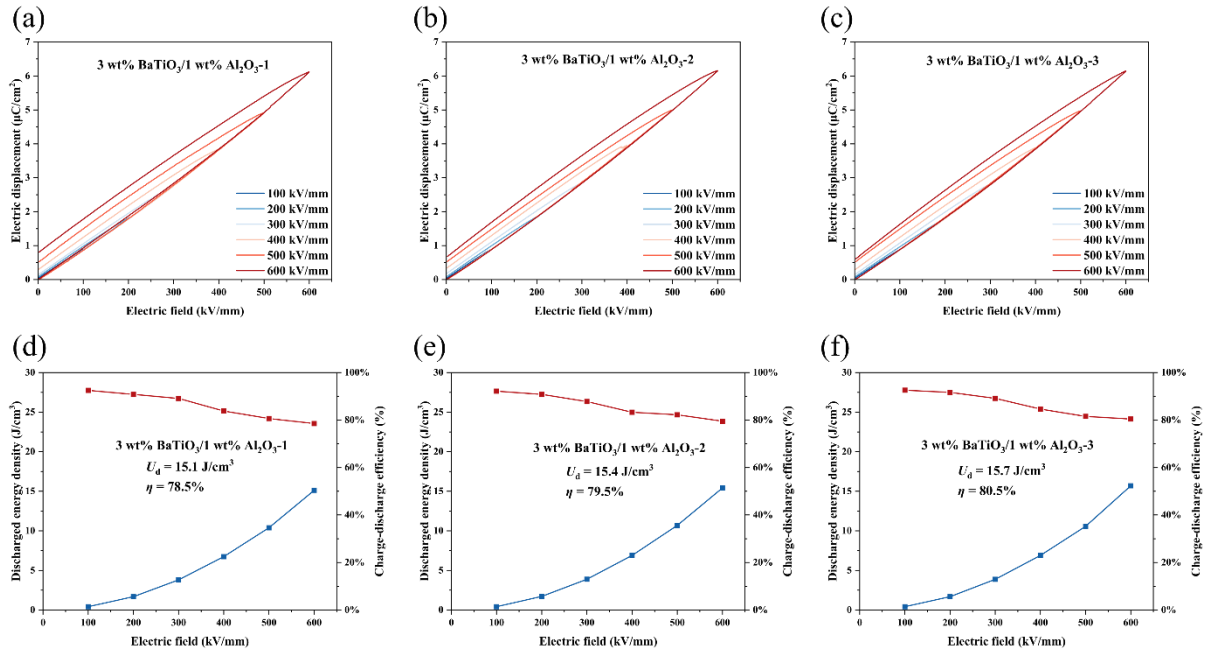

Fig. S35. (a-c) *D-E* curves and (d-f) discharged energy density and charge-discharge efficiency of the core co-doped dielectric 3 wt% $BaTiO_3$/1 wt% Al_2O_3.

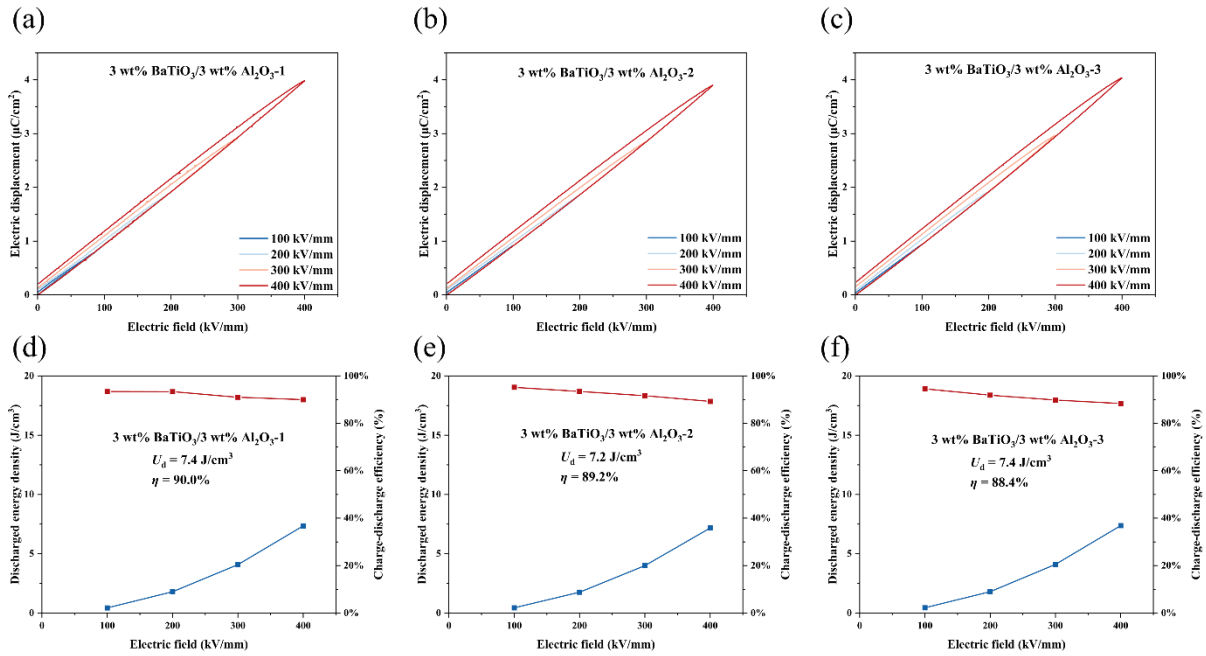

Fig. S36. (a-c) *D-E* curves and (d-f) discharged energy density and charge-discharge efficiency of the core co-doped dielectric 3 wt% $BaTiO_3$/3 wt% Al_2O_3.

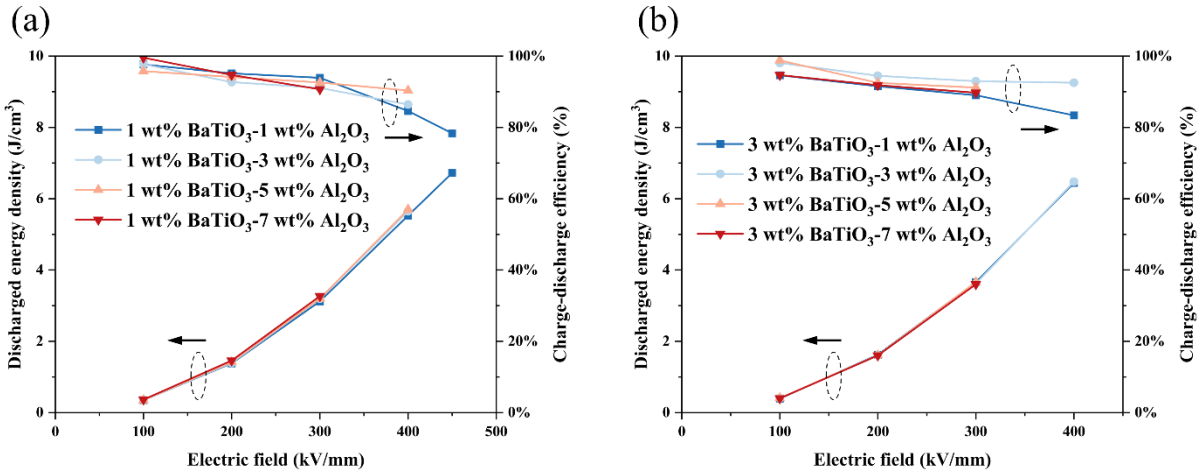

Fig. S37. Discharged energy density and charge-discharge efficiency of layer-doped dielectrics.

Table S8. Comparison of key dielectric parameters in this work and previous literature reports.

Materials	category	ε_r@1 kHz	E_b (kV/mm)	U_d (J/cm^3)	η (%)	Frequency	Temperature
5vol%BTO/P(VDF-HFP)[1]	Organic/ inorganic composite	14.2	676	18	65%	10 Hz	RT
(0.1wt%)TiO_2@Au/PVDF[2]		10.4	750	18.6	70.3%	100 Hz	RT
180° BT@SO/PVDF[3]		9.1	650	20.6	54%	10 Hz	RT
P(VDF)/BNNS/P(VDF)[4]		11.5	612	14.3	70%	10 Hz	RT
PS-b-P4VP(PDP)/9 vol% ZrO_2[5]		3.6	650	6.2	90%	100 Hz	RT
PVDF/SBNO/PVDF-7[6]		11.2	508	12.8	64.5%	100 Hz	RT
PVDF-BT/PVDF-Mica/PVDF-BT[7]		20	350	11.48	50.8%	-	RT
PMF20[8]	All Organic	3.3	625	9.6	90.9%	10 Hz	RT
PEI/PEI-P(VDF-HFP)/P(VDF-HFP)[9]		5.4	535	12.2	89.9%	100 Hz	RT
PVDF@Chitosan (0.8wt%) [10]		6.3	630	10.1	72%	-	RT
POFNB[11]		2.5	700	6.5	96.5%	100 Hz	RT
γ-150 kGy BOPP[12]		2.4	968	10.4	97.3%	10 Hz	RT
1 wt% $BaTiO_3$/1 wt% Al_2O_3 (This work)		5.0	619	19.1	80%	100 Hz	RT

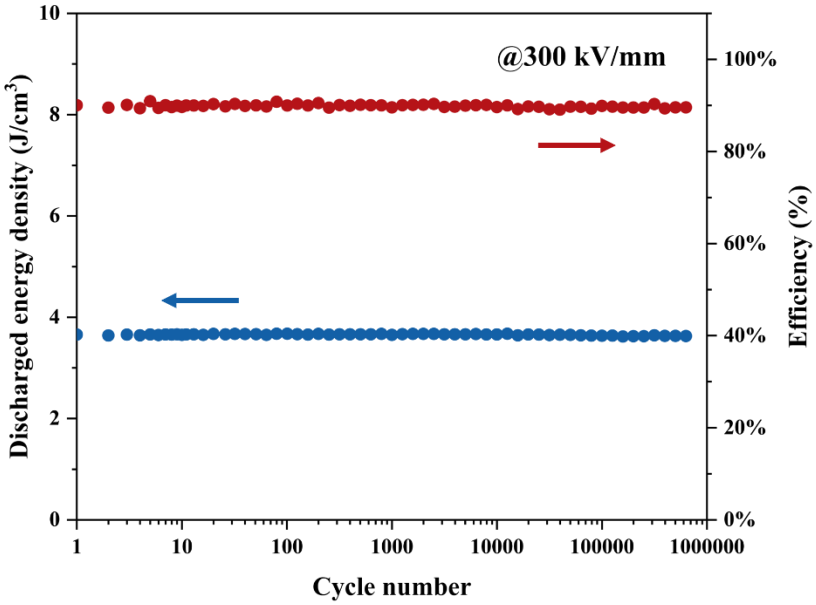

Fig. S38. Charge-discharge cycle stability of 1 wt% $BaTiO_3$/1 wt% Al_2O_3 dielectric at 300 kV/mm

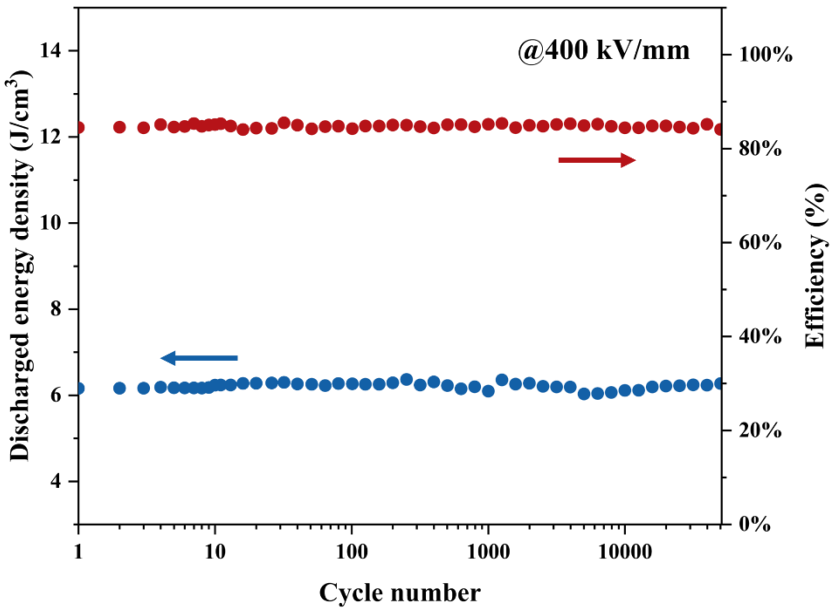

Fig. S39. Charge-discharge cycle stability of 1 wt% $BaTiO_3$/1 wt% Al_2O_3 dielectric at 400 kV/mm after thermal cycling.

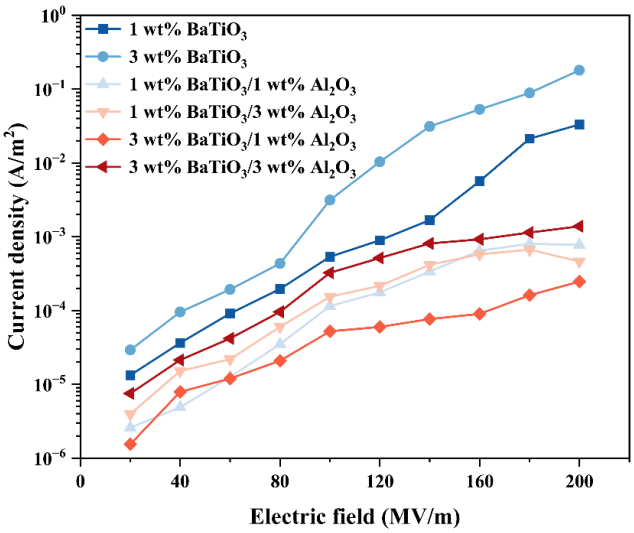

Fig. S40. Leakage current density of core-doped $BaTiO_3$ dielectrics and core co-doped dielectrics.

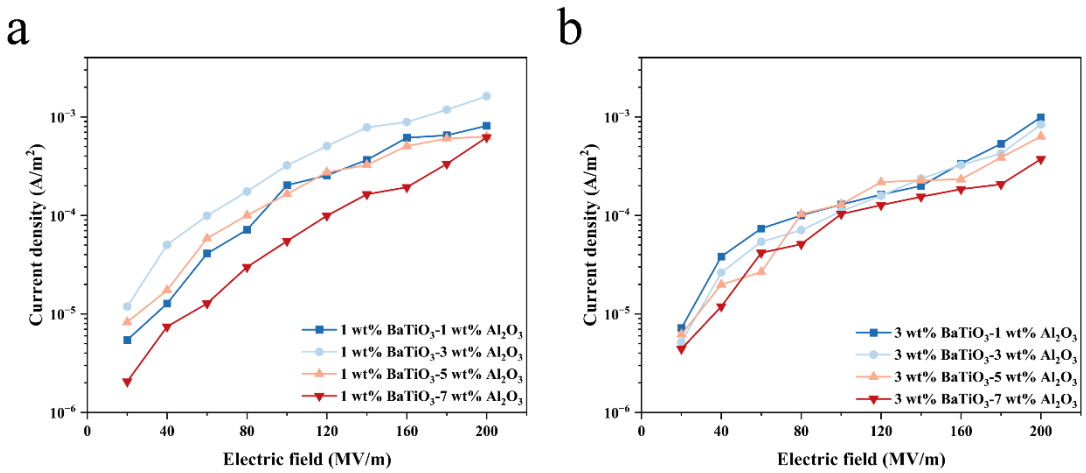

Fig. S41. Leakage current density of layered-doped dielectrics: (a) 1 wt% $BaTiO_3$-*x* wt% Al_2O_3 and (b) 3 wt% $BaTiO_3$-*x* wt% Al_2O_3.

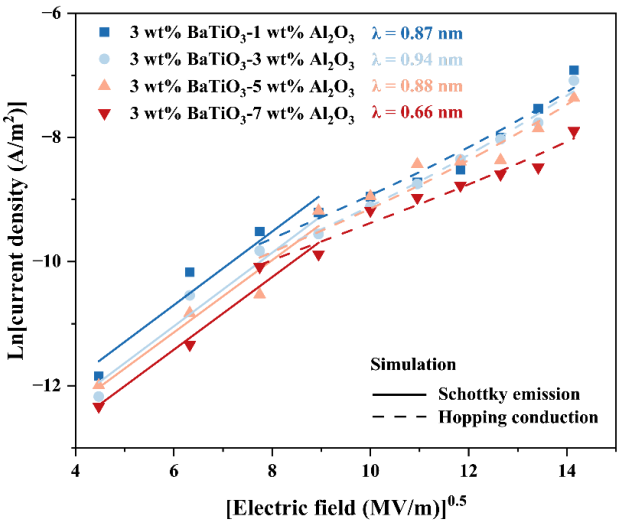

Fig. S42. Leakage current fitting of layered-doped dielectrics based on the Schottky emission and hopping conductance models.

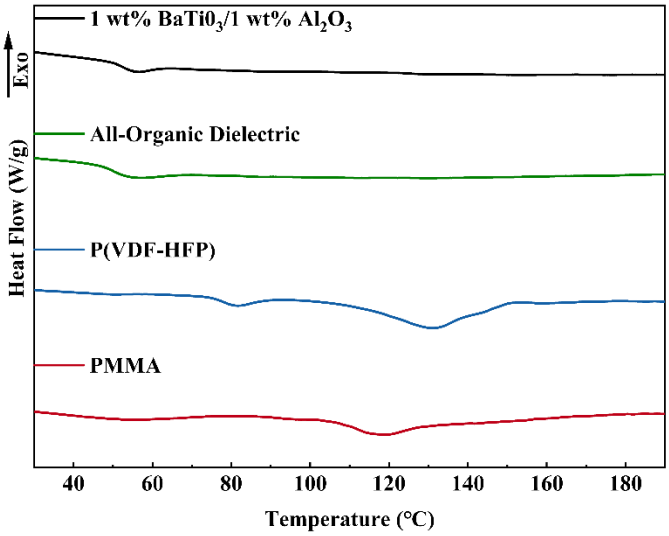

Fig. S43. Young's modulus of all-organic dielectric and 1 wt% $BaTiO_3$/1 wt% Al_2O_3 dielectric.

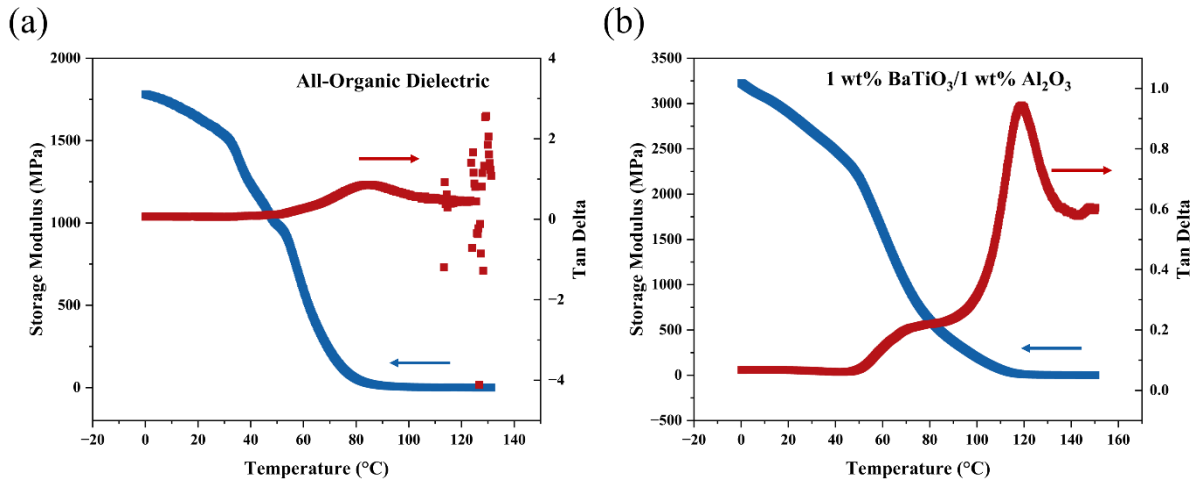

Fig. S44. Dynamic Mechanical Analysis of all-organic dielectric and 1 wt% $BaTiO_3$/1 wt% Al_2O_3 dielectric.

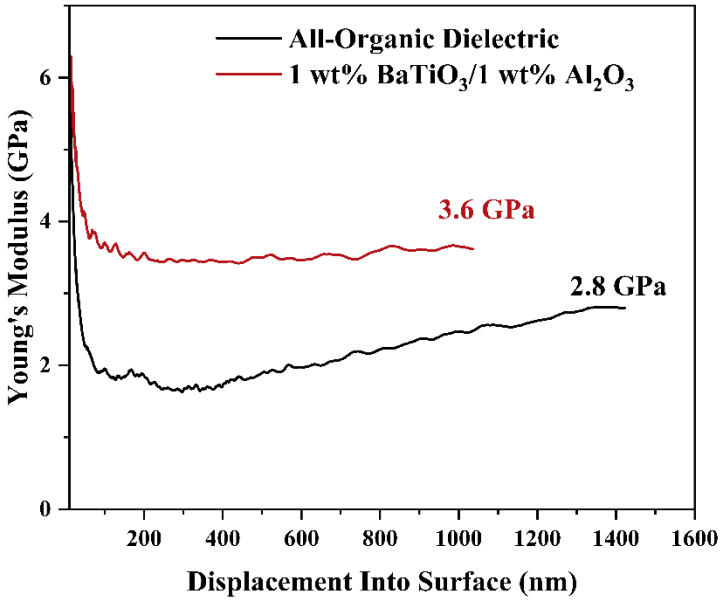

Fig. S45. Young's modulus of all-organic dielectric and 1 wt% $BaTiO_3$/1 wt% Al_2O_3 dielectric.

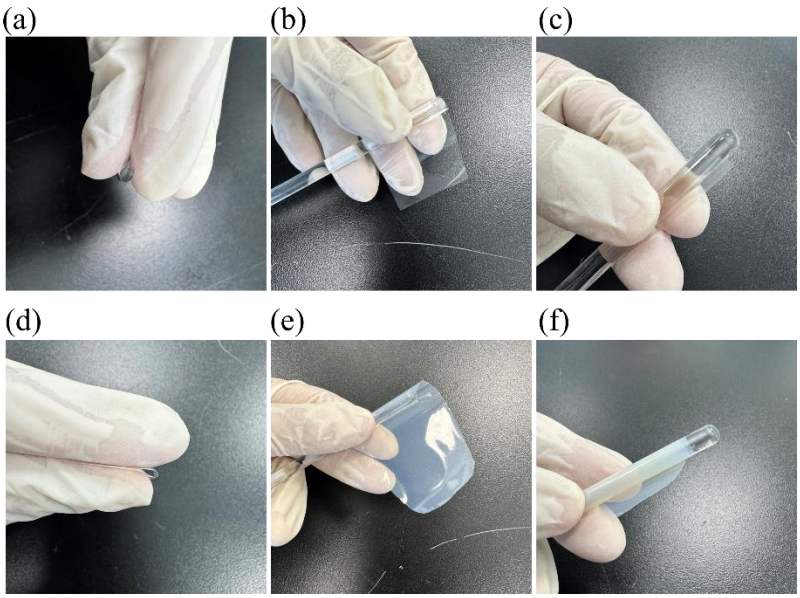

Fig. S46. Flexibility of all-organic dielectrics (a-c) and 1 wt% $BaTiO_3$/1 wt% Al_2O_3 dielectric (d-f).

Table S9. Density of the all-organic dielectric and 1 wt% $BaTiO_3$/1 wt% Al_2O_3 dielectric

	Density (g/cm^3)
All-organic dielectric	0.1431
1 wt% $BaTiO_3$/1 wt% Al_2O_3 dielectric	0.1445

Supplementary Notes

Supplementary Note 1. Conduction in the lower electric field regime

In the lower electric field regime discussed in Figs. 4a, 4b and S18, we assign the Schottky emission the most plausible conduction mechanism. In this case, carriers can overcome the energy barrier at the electrode/dielectric interface and be injected into the dielectric. As the electric field is increased, the barrier height is lowered due to the superposition of the image charge potential with the external potential. The Schottky emission[13] based on leakage density (J) and electric field (E) can be expressed by

$$J = AT^2\, exp\left[-\left(\frac{\varphi-\sqrt{e^3/4\pi\varepsilon}\sqrt{E}}{K_B T}\right)\right] \quad (1)$$

where E is the electric field, A the Richardson constant, φ the barrier height at the electrode/dielectric interface, T the temperature, ε the dielectric constant, and K_B the Boltzmann constant. Supplementary Eq. (1) can be rewritten as

$$ln(J) = \left(\frac{\sqrt{e^3/4\pi\varepsilon}}{K_B T}\right)\sqrt{E} + ln(AT^2) - \left(\frac{\varphi}{K_B T}\right) \quad (2)$$

From Supplementary Eq. (2), the plot of ln(J) versus$\sqrt{E}$ shall exhibit a linear relationship. The dielectric constant derived from the slope of fitted curve can be used to determine whether the conduction mechanism in the dielectric conforms to the Schottky emission. The calculated dielectric constant of the organic-inorganic composite dielectric are shown in Table S2, very close to the experimental data, suggesting that Schottky emission is the main conduction mechanism in the low field region.

Table S10. The calculated dielectric constant of the organic-inorganic composite dielectric.

Dielectrics	ε_r	Dielectrics	ε_r
1 wt% $BaTiO_3$	6.0	1 wt% $BaTiO_3$-1 wt% Al_2O_3	6.1
3 wt% $BaTiO_3$	6.2	1 wt% $BaTiO_3$-3 wt% Al_2O_3	6.1
1 wt% $BaTiO_3$/1 wt% Al_2O_3	6.5	1 wt% $BaTiO_3$-5 wt% Al_2O_3	6.4
1 wt% $BaTiO_3$/3 wt% Al_2O_3	6.6	1 wt% $BaTiO_3$-7 wt% Al_2O_3	6.5
3 wt% $BaTiO_3$/1 wt% Al_2O_3	6.8	3 wt% $BaTiO_3$-1 wt% Al_2O_3	6.2
3 wt% $BaTiO_3$/3 wt% Al_2O_3	7.0	3 wt% $BaTiO_3$-3 wt% Al_2O_3	6.2
		3 wt% $BaTiO_3$-5 wt% Al_2O_3	6.5
		3 wt% $BaTiO_3$-7 wt% Al_2O_3	6.4

Supplementary Note 2. Conduction in the higher electric field regime

In the higher electric field regime discussed in in Figs. 4a, 4b and S18, we assign the hopping conduction[14] the most plausible mechanism. The hopping conduction is a bulk mechanism that models the movement of individual carriers, assumed to be electrons, through the material. The carriers gain energy through random thermal fluctuations and phonon interaction to escape their localized state and travel in an extended state for a small amount of time before being recaptured by another localized state.

$$J = n_c 2v\lambda \mathrm{e} * \exp\left(-\frac{W_\mathrm{a}}{K_\mathrm{B}T}\right) \sinh\left(\frac{\lambda \mathrm{e}E}{2K_BT}\right) \quad (3)$$

where n_c is the carrier concentration, λ the hopping distance, v the attempt-to-escape frequency, W_a the activation energy in eV, e the charge of the carriers, T the temperature, K_B the Boltzmann constant. Fitting the ln(J)-$E^{0.5}$ data to the hopping conduction model gives the hopping distance λ (i.e., mean spacing between trap sites). From Supplementary Eq. (3), the plot of ln(J) versus $E^{0.5}$ shall exhibit a hyperbolic sine relationship. The hopping distance λ for different composite dielectrics are shown in Table S3.

Table S11. Calculated jump distance (λ) of organic-inorganic composite dielectric.

Dielectric	λ (nm)	Dielectric	λ (nm)
1 wt% $BaTiO_3$	2.21	1 wt% $BaTiO_3$-1 wt% Al_2O_3	1.05
3 wt% $BaTiO_3$	2.57	1 wt% $BaTiO_3$-3 wt% Al_2O_3	0.95
1 wt% $BaTiO_3$/1 wt% Al_2O_3	1.53	1 wt% $BaTiO_3$-5 wt% Al_2O_3	0.83
1 wt% $BaTiO_3$/3 wt% Al_2O_3	1.12	1 wt% $BaTiO_3$-7 wt% Al_2O_3	1.31
3 wt% $BaTiO_3$/1 wt% Al_2O_3	0.98	3 wt% $BaTiO_3$-1 wt% Al_2O_3	0.87
3 wt% $BaTiO_3$/3 wt% Al_2O_3	1.21	3 wt% $BaTiO_3$-3 wt% Al_2O_3	0.94
		3 wt% $BaTiO_3$-5 wt% Al_2O_3	0.88
		3 wt% $BaTiO_3$-7 wt% Al_2O_3	0.66

Supplementary Note 3. Finite element simulation of electric branch distribution

The real-time evolutions of the electric tree path development in the core-doped $BaTiO_3$ dielectrics, the layered-doped dielectrics and the core co-doped dielectrics were simulated using COMSOL Multiphysics 6.3. For the whole simulations, the width and height of cross-sections of composite films are respectively set to 20 μm, in order to match the actual dimensions of test samples. The original value of dielectric constants (ε_r) of $BaTiO_3$, Al_2O_3, PMMA, and P(VDF-HFP) are respectively set to 300, 12, 4, 10. The dielectric constant is set to change with the degree of damage to the material: $\varepsilon_s = \frac{\varepsilon_r}{f(s)+10^{-4}}$. Where ε_r and ε_s are the initial dielectric constant and the real-time dielectric constant, respectively, and *f(s)* is the effect of material damage on its electrical properties, satisfying $f(s) = 4\times s^3-3\times s^4$. s is a function representing the degree of material damage, ranging from 0 to 1. $s = 1$ indicates that the material is intact, while $s = 0$ indicates that the material is completely damaged.

The failure state of the material is determined using an energy-based criterion. Specifically, the total energy functional of the system-including the electrostatic energy, the damage energy, and the gradient energy associated with the diffuse interface-is evaluated. When the total energy exceeds the intrinsic damage dissipation energy (breakdown energy) of the material, failure initiates and subsequently evolves at a finite rate. The temporal evolution of material degradation is governed by the following relation:

$$\frac{1}{\alpha}\frac{\partial s}{\partial t} = -\frac{f\prime(s)}{2[f(s)+10^{-4}]^2}\frac{\partial \phi}{\partial x_i}\frac{\partial \phi}{\partial x_i} + f'(s) + \frac{1}{2}\frac{\partial^2 s}{\partial x_i \partial x_i} \quad (4)$$

Here, ϕ denotes the electrostatic potential at a given point within the material. The above equation is expressed in a normalized form, where α is the normalized resul, calculated based on the material's relative permittivity and its damage dissipation energy. For computational convenience, the α values used for different materials in this model are summarized in the table below:

Table S12. The α values used for different materials.

Materials	PMMA	P(VDF-HFP)	$BaTiO_3$	Al_2O_3
α	1	0.8	5	1.3

Supplementary Note 4. Surface free energy measurement of solid particles.

The surface free energy of the solid particles was determined from contact-angle measurements using the Owens-Wendt-Rabel-Kaelble (OWRK) method. In this approach, two probe liquids with known surface-tension components, namely deionized water and hexadecane, were used to determine the total surface free energy and its dispersive and polar components.

According to the OWRK model, the contact angle satisfies:

$$\gamma_l(1+\cos\theta) = 2\sqrt{\gamma_s^d \gamma_l^d} + 2\sqrt{\gamma_s^p \gamma_l^p} \tag{5}$$

Where γ_l is the total surface tension of the probe liquid, γ_l^d and γ_l^p are the dispersive and polar components of the liquid surface tension, respectively, γ_s^d and γ_s^p are the dispersive and polar components of the solid surface free energy, and θ is the measured contact angle. The total surface free energy of the solid is given by:

$$\gamma_s = \gamma_s^d + \gamma_s^p \tag{6}$$

Contact-angle measurements were performed using a JY-82C video contact-angle measurement system (Chengde Dingsheng, China) with an angular resolution of 0.01°. For each measurement, a 1 μL droplet of water or hexadecane was deposited onto the solid surface, and the static contact angle was recorded. The dispersive and polar components of the solid surface free energy were then calculated from the measured contact angles using the OWRK model.

Supplementary Note 5. Surface tension measurement by the pendant drop method.

The surface tension of the liquid was measured by the pendant drop method, which is based on the Young-Laplace equation. In this method, a liquid droplet is suspended from the tip of a needle, and its equilibrium profile is determined by the balance between surface tension and gravity. The pressure difference across the curved interface satisfies:

$$\Delta P = \gamma(\frac{1}{R_1} + \frac{1}{R_2}) \tag{7}$$

where ΔP is the pressure difference across the interface, γ is the surface tension, and R_1 and R_2 are the two principal radii of curvature of the droplet surface.

Under gravitational force, the pressure difference also varies with vertical position:

$$\Delta P = \Delta P_0 + \Delta\rho g z \tag{8}$$

where ΔP_0 is the pressure difference at the droplet apex, $\Delta\rho$ is the density difference between the liquid and the surrounding phase, g is the gravitational acceleration, and z is the vertical distance from the apex.

By combining the above equations, the droplet profile can be described by the Bashforth-Adams equation. In practical measurement, the entire droplet contour is recorded and fitted to the theoretical Young-Laplace profile. The surface tension is then obtained from:

$$\gamma = \frac{\Delta\rho g b^2}{\beta} \tag{9}$$

where b is the radius of curvature at the droplet apex, and β is the dimensionless shape factor obtained from profile fitting.

Supplementary Note 6. Determination of the polar and dispersive components of liquid surface tension from liquid-liquid interfacial tension measurements.

The liquid-liquid interfacial tension was measured by the pendant drop method, which is based on the Young-Laplace equation. For a droplet suspended in another liquid phase, the pressure difference across the curved interface satisfies:

$$\Delta P = \gamma_{12}(\frac{1}{R_1} + \frac{1}{R_2}) \tag{10}$$

where ΔP is the pressure difference across the interface, γ_{12} is the liquid-liquid interfacial tension, and R_1 and R_2 are the two principal radii of curvature. For an axisymmetric pendant drop at mechanical equilibrium, the drop profile can be described by the Bashforth-Adams equation**:**

$$2 - \beta\left(\frac{z}{b}\right) = \frac{1}{R/b} + \frac{sin\phi}{x/b} \tag{11}$$

where b is the radius of curvature at the drop apex, R is the principal radius of curvature at a point on the profile, ϕ is the angle between the tangent and the horizontal axis, and β is the Bond number (shape factor). The Bond number is defined as:

$$\beta = \frac{b^2 \Delta\rho g}{\gamma_{12}} = \frac{b^2}{\alpha^2} \tag{12}$$

and the capillary constant is:

$$\alpha = \sqrt{\frac{\gamma_{12}}{\Delta\rho g}} \tag{13}$$

where $\Delta\rho$ is the density difference between the two liquid phases and g is the gravitational acceleration. In practice, the full droplet contour is fitted to the theoretical Young-Laplace profile to obtain α, from which the interfacial tension is calculated.

After obtaining the interfacial tension between the test liquid and a reference liquid with known surface-tension components, the dispersive and polar components of the test liquid surface tension can be determined using a component-based interfacial-tension model. In this work, the Owens-Wendt approach was used, in which the total surface tension of a liquid is expressed as:

$$\gamma = \gamma^d + \gamma^p \tag{14}$$

where γ^d and γ^p are the dispersive and polar components, respectively.

The interfacial tension between two liquids 1 and 2 is then written as:

$$\gamma_{12} = \gamma_1 + \gamma_2 - 2(\sqrt{\gamma_1^d \gamma_2^d} + \sqrt{\gamma_1^p \gamma_2^p}) \quad (15)$$

If the total surface tension of liquid 1 is known,

$$\gamma_1 = \gamma_1^d + \gamma_1^p \quad (16)$$

and the total surface tension and components of reference liquid 2 are known, then γ_1^d and γ_1^p can be obtained by solving the above equations together with the measured γ_{12}. For a nonpolar reference liquid such as hexadecane, $\gamma_2^p = 0$, and the interfacial-tension equation becomes:

$$\gamma_{12} = \gamma_1 + \gamma_2 - 2\sqrt{\gamma_1^d \gamma_2^d} \quad (17)$$

Supplementary References

1 Jiang, Y. *et al.* Ultrahigh breakdown strength and improved energy density of polymer nanocomposites with gradient distribution of ceramic nanoparticles. *Adv. Funct. Mater.* **30**, 1906112 (2020).

2 Ren, Z. L. *et al.* Core-shell TiO_2@Au nanofibers derived from a unique physical coating strategy for excellent capacitive energy storage nanocomposites. *Adv. Funct. Mater.* **34**, 2401907 (2024).

3 Wang, F. *et al.* Surface-confined winding assembly of SiO_2 on the surface of $BaTiO_3$ leading to enhanced performance of dielectric nanocomposites. *Adv. Funct. Mater.* **34**, 2410862 (2024).

4 Zhu, Y. K. *et al.* High energy density polymer dielectrics interlayered by assembled boron nitride nanosheets. *Adv. Energy Mater.* **9**, 1901826 (2019).

5 Li, H. *et al.* Multilaminate energy storage films from entropy-driven self-assembled supramolecular nanocomposites. *Adv. Mater.* **36**, 2401954 (2024).

6 Ryu, A. *et al.* Layer-controlled perovskite 2D nanosheet interlayer for the energy storage performance of nanocomposites. *Small* **19**, 2300526 (2023).

7 Ren, Y. J. *et al.* Significantly enhanced the energy density of dielectric composites by sandwich structure with highly insulating mica nanosheets. *Small* **20**, 2308276 (2024).

8 Li, D. L. *et al.* Scalable in-situ microfibrillar dielectric films: Achieving exceptional energy density and efficiency. *Energy Storage Mater.* **72**, 103717 (2024).

9 Sun, L. *et al.* Asymmetric trilayer all-polymer dielectric composites with simultaneous high efficiency and high energy density: A novel design targeting for advanced energy storage capacitors. *Adv. Funct. Mater.* **31**, 2100280 (2021).

10 Che, J. J. *et al.* High-energy-density waterborne dielectrics from polyelectrolyte-colloid complexes. *Adv. Funct. Mater.* **33**, 2213804 (2023).

11 Wu, C. *et al.* Flexible temperature-invariant polymer dielectrics with large bandgap. *Adv. Mater.* **32**, 2000499 (2020).

12 Wang, Y. W. *et al.* γ-Ray irradiation significantly enhances capacitive energy storage

performance of polymer dielectric films. *Adv. Mater.* **36**, 2308597 (2024).

13 Barth, S. *et al.* Current injection from a metal to a disordered hopping system.: III.: Comparison between experiment and Monte Carlo simulation. *Phys. Rev. B* **60**, 8791-8797 (1999).

14 Nemeth, R. & Muhlschlegel, B. Hopping Hall conductivity in disordered and granular systems. *Solid State Commun.* **66**, 999-1001 (1988).